

# A THEORETICALLY-PRINCIPLED SPARSE, CONNECTED, AND RIGID GRAPH REPRESENTATION OF MOLECULES

**Anonymous authors**

Paper under double-blind review

## ABSTRACT

Graph neural networks (GNNs) – learn graph representations by exploiting graph’s sparsity, connectivity, and symmetries – have become indispensable for learning geometric data like molecules. However, the most used graphs (e.g., radial cutoff graphs) in molecular modeling lack theoretical guarantees for achieving connectivity and sparsity simultaneously, which are essential for the performance and scalability of GNNs. Furthermore, existing widely used graph construction methods for molecules lack rigidity, limiting GNNs’ ability to exploit graph nodes’ spatial arrangement. In this paper, we introduce a new hyperparameter-free graph construction of molecules and beyond with sparsity, connectivity, and rigidity guarantees. Remarkably, our method consistently generates connected and sparse graphs with the edge-to-node ratio being bounded above by 3. Our graphs’ rigidity guarantees that edge distances and dihedral angles are sufficient to uniquely determine general spatial arrangements of atoms. We substantiate the effectiveness and efficiency of our proposed graphs in various molecular modeling benchmarks.

## 1 INTRODUCTION

Graph neural networks (GNNs) have emerged as indispensable tools for learning graphs, e.g., social networks (Perozzi et al., 2014) and molecules (Duvenaud et al., 2015; Gilmer et al., 2017; Townshend et al., 2021; Merchant et al., 2023). GNNs operate by exchanging messages between neighboring nodes for learning features at both node and graph levels; see, e.g. (Kipf & Welling, 2017; Gilmer et al., 2017; Satorras et al., 2021). Constructing sparse and connected graph representations of the input data plays a pivotal role in the success of GNNs, especially in molecular modeling and beyond. Graph sparsity enables computational efficiency, and connectivity ensures that information can flow seamlessly throughout the network – it has been shown that the disconnectivity of a graph can degrade the model’s performance; see, e.g., (Sverdlov & Dym, 2024).

A common method for creating molecular graphs involves setting a radial cutoff distance; atoms are connected by edges if their Euclidean distance falls below the cutoff threshold (Schütt et al., 2017; 2018; Unke & Meuwly, 2019). To limit the number of connections per atom, ad-hoc post-pruning can be applied, removing edges between distant atoms if a node has too many connections. However, determining an optimal radial cutoff for molecular graphs presents a significant challenge. A large cutoff might guarantee that all atoms are connected, but it can result in overly dense graphs. Conversely, while post-pruning can reduce the density of graphs, it might introduce the risk of disconnectivity. Furthermore, for large molecules like proteins with thousands of atoms, a fixed cutoff is often insufficient to ensure connectivity. Examples include long-range atomic interactions in protein allosteric regulation (Süel et al., 2003; Zhu et al., 2022) and inter-chain interactions in protein oligomerization (Chen et al., 2021; Chen & Bell, 2021). To illustrate the limitations of the radial cutoff method, we present Fig. 1(a), which depicts a protein molecule with colored residues. These colored residues represent a single instance from the Fold biomolecule dataset (Murzin et al., 1995; Hou et al., 2018). As shown in Fig. 1(b), applying a cutoff of  $10\text{\AA}$  on the data consisting of  $C_\alpha$  atoms of amino acids results in a disconnected but quite dense graph. To further solidify the challenges in balancing sparsity and connectivity using radial cutoff graphs, we investigate the sparsity and connectivity tradeoff using various cutoff thresholds to construct graphs for proteins in the Fold dataset. Next, for these radial cutoff graphs, we calculate the edge-to-node ratio and the proportion of connected graphs for different cutoff thresholds. As shown in Fig. 1(e), a cutoff of  $48\text{\AA}$  is required to achieve connectivity for large proteins with more than 1000 amino acids. However, as shown in Fig. 1(d), connectivity comes at the cost of dramatically increased density, e.g., a cutoff of

054  
055  
056  
057  
058  
059  
060  
061  
062  
063  
064  
065  
066  
067  
068  
069  
070  
071  
072  
073  
074  
075  
076  
077  
078  
079  
080  
081  
082  
083  
084  
085  
086  
087  
088  
089  
090  
091  
092  
093  
094  
095  
096  
097  
098  
099  
100  
101  
102  
103  
104  
105  
106  
107

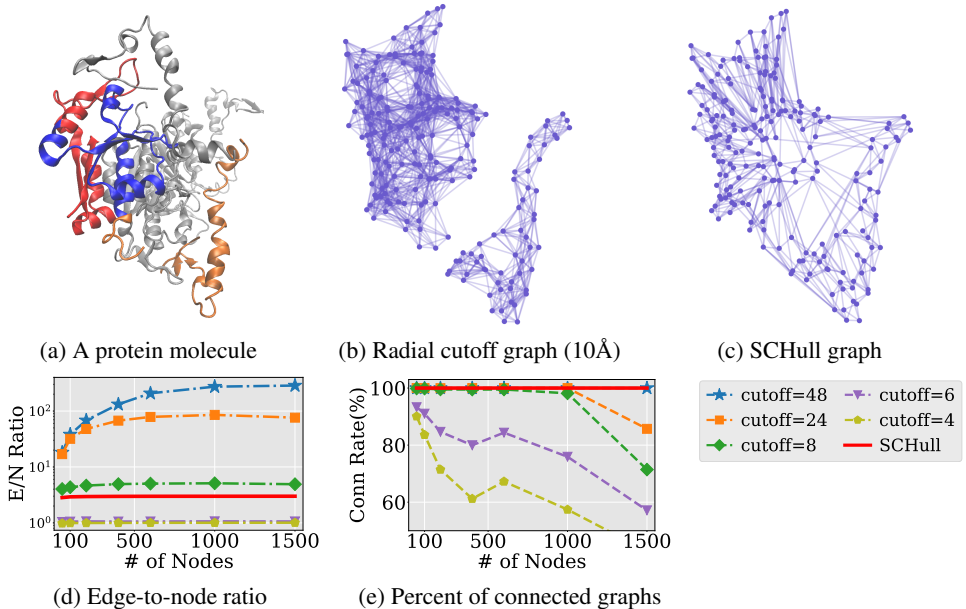


Figure 1: Illustration of challenges of radial cutoff graphs in balancing sparsity and connectivity for the Fold biomolecule dataset. (a) Colored residues in a large protein, representing a single instance from the Fold dataset. (b) A radial cutoff graph with a cutoff of 10Å for the colored residues, demonstrating disconnection and density; in contrast, (c) showcases our proposed SCHull graphs, ensuring sparsity and connectivity. Panels (d) and (e) plot the number of nodes against the edge-to-node ratio and the percentage of connected graphs, respectively, for radial cutoff graphs using different thresholds and our SCHull graph construction. The results highlights that radial cutoff has to trade sparsity for connectivity, while our SCHull graphs maintain both properties.

48Å results in graphs with over 100 times more edges than graphs constructed with a 6Å cutoff. We further discuss other popular graph representations of molecules like chemical graphs and  $k$ -nearest neighbor graphs in Section 2.

Besides sparsity and connectivity, it’s essential to consider whether a geometric graph could contain sufficient information to determine its nodes’ spatial arrangement (geometries). Pairwise distances between all nodes theoretically determine the geometric arrangement (Satorras et al., 2021) up to rigid motions, but computing pairwise distances between all nodes amounts to involving a dense graph in the operation. Alternatively, researchers have explored sparse edge distributions with specific geometric features to identify the spatial arrangement of graph nodes. Sverdlov & Dym (2024) connect identifying nodes’ arrangement to graph rigidity and have demonstrated that graph rigidity can ensure a GNN’s ability to distinguish general geometric configurations of nodes. Nevertheless, radial cutoff graphs often lack sufficient rigidity, leading to ambiguity in spatial arrangements (Joshi et al., 2023; Wang et al., 2024). Figure 2 illustrates this limitation using a synthetic example: A and B are two distinct, non-isometric arrangements of five points in Euclidean space; while applying a radial cutoff to these arrangements results in connected and sparse graphs. However, the edges in both graphs have the same lengths, making it challenging for GNNs to distinguish between them.

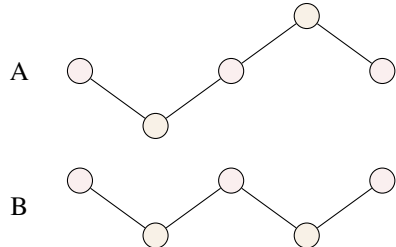


Figure 2: Illustration of two distinct, non-isometric arrangements of nodes in Euclidean space. When applying a radial cutoff to the arrangements in A and B, we obtain connected and sparse graphs. However, the corresponding edges in both graphs have identical lengths, making it challenging for graph neural networks to distinguish between them.

### 1.1 OUR CONTRIBUTIONS

In response to the limitation of existing graph constructions of molecules, we propose Spherical Convex Hull (SCHull) – a new hyperparameter-free graph construction method tailored for data with 3D coordinates, especially molecules. SCHull constructs graph representations of the underlying points in two computationally efficient steps: (1) project points onto the unit sphere centered at the center of points, and (2) construct a convex hull for the projected points and add an edge to connect two original points if the convex hull has an edge connecting the corresponding projected points; see details in Section 3.1. SCHull graphs enjoy a few advantages with theoretical guarantees:

- SCHull graphs are connected and sparse. In particular, the edge-to-node ratio is bounded above by 3; see detailed theoretical results in Section 3.2.
- SCHull graph mirrors the spatial arrangement of the underlying point clouds, ensuring that encoding edge distances and dihedral angles are sufficient for GNNs to uniquely determine the geometric configurations of nodes up to isometries; see Section 3.3 for details.

Furthermore, the SCHull graph can be seamlessly coupled with existing GNN learning techniques to boost the performance of off-the-shelf models. We substantiate the effectiveness and efficiency of the proposed SCHull graph using a few molecular modeling benchmarks, including predicting atomic forces for small chemicals, protein fold classification, enzyme reaction classification, and protein-ligand binding affinity prediction; see details in Section 4. Our numerical results show that using SCHull can consistently improve the prediction accuracy of existing remarkable GNNs by a significant margin at the cost of a tiny computational overhead.

## 1.2 ORGANIZATION

We organize this paper as follows: In Section 2, we recap on necessary background materials and some related results. We present the construction process of our proposed SCHull graphs in Section 3.1, followed by their sparsity and connectivity analysis in Section 3.2. We further analyze the rigidity of SCHull graphs and their benefits in improving GNN’s performance in Section 3.3. We substantiate the performance of SCHull in Section 4 using various benchmark tasks in molecular modeling. Technical proofs and additional experimental details are provided in the appendix.

## 2 BACKGROUND AND SOME RELATED WORKS

In this section, we aim to provide a brief review of some crucial concepts and related results. In particular, we recall some concepts of geometric graphs discussed by Joshi et al. (2023); Wang et al. (2024), some existing graph construction methods for molecules, and the definition of graph rigidity and generic point clouds studied by Sverdllov & Dym (2024). For a more in-depth understanding of graph rigidity, we refer readers to (Asimow & Roth, 1978; Connelly, 2005). Furthermore, we will recap on message-passing GNNs and their separation power.

**Point clouds and geometric graphs.** A 3D *point cloud*, consisting of  $m$  points  $\mathbf{x}_1, \mathbf{x}_2, \dots, \mathbf{x}_m$ , can be viewed as a spatial arrangement of a set of  $m$  nodes  $\mathcal{V} = \{1, 2, \dots, m\}$ , where each index  $i$  is associated with a node with coordinate  $\mathbf{x}_i \in \mathbb{R}^3$ . We can represent a point cloud as a set  $\{\mathbf{x}_i\}_{i=1}^m$  or as a spatial arrangement of nodes  $(\mathcal{V}, \mathbf{X} = [\mathbf{x}_1, \mathbf{x}_2, \dots, \mathbf{x}_m])$ . Optionally, each node may be associated with features  $\mathbf{f}_i \in \mathbb{R}^{n_f}$  beyond coordinates. Extending from a point cloud to a *geometric graph* – denoted as  $\mathcal{G} = (\mathcal{V}, \mathcal{E}, \mathbf{X})$  (resp.  $(\mathcal{V}, \mathcal{E}, \mathbf{X}, \mathbf{F})$ ) – introduces a graph structure by connecting nodes using edges in the set  $\mathcal{E}$  to include relationships between points in  $(\mathcal{V}, \mathbf{X})$  (resp.  $(\mathcal{V}, \mathbf{X}, \mathbf{F})$ ). Here,  $(i, j) \in \mathcal{E}$  denotes an edge and  $\mathbf{F} = [\mathbf{f}_1, \dots, \mathbf{f}_m]$  represents node features.

**Existing graph representations of molecules.** As mentioned earlier, radial cutoff is one of the prevailing approaches to construct graph representations of molecules. Besides radial cutoff, there are several other methods have also been used to construct graphs for molecules, including  $k$ -nearest neighbor graphs ( $k$ NN) (Jørgensen et al., 2018) and chemical graphs (Gilmer et al., 2017). Similar to the radial cutoff graphs,  $k$ -nearest neighbor graphs and chemical graphs also struggle to achieve sparsity, connectivity, and rigidity at the same time; we contrast different graphs’ properties in Table 1.

Table 1: Contrasting different graph construction methods in achieving sparsity, connectivity, and rigidity.

Construction method	Sparsity	Connectivity	Rigidity
Radial cutoff (small threshold)	✓	✗	✗
Radial cutoff (large threshold)	✗	✓	✓
$k$ -nearest neighbors	✓	✗	✗
Chemical graphs	✓	✓	✗
SCHull (ours)	✓	✓	✓

**Rigid motions and geometric isomorphism.** A *rigid motion*, a.k.a. an *isometry*, is a transformation defined by an orthogonal matrix  $\mathbf{Q} \in \text{O}(3)$  and a translation vector  $\mathbf{t} \in \mathbb{R}^3$ . It acts on the point cloud by transforming all its points according to  $\mathbf{x}_i \mapsto \mathbf{Q}\mathbf{x}_i + \mathbf{t}$ . The group of 3D rigid motions is called the Euclidean group and is denoted by  $\text{E}(3)$ . Two geometric graphs  $\mathcal{G}_1 = (\mathcal{V}_1, \mathcal{E}_1, \mathbf{X}_1, \mathbf{F}_1)$  and  $\mathcal{G}_2 = (\mathcal{V}_2, \mathcal{E}_2, \mathbf{X}_2, \mathbf{F}_2)$  are said to be *geometrically isomorphic if and only if* there exists a bijection  $b: \mathcal{V}_1 \rightarrow \mathcal{V}_2$  and a rigid motion  $(\mathbf{Q}, \mathbf{t}) \in \text{E}(3)$  such that for any  $(i, j) \in \mathcal{E}_1$ ,  $(b(i), b(j)) \in \mathcal{E}_2$ , and for any  $i$ ,  $\mathbf{f}_i = \mathbf{f}_{b(i)}$ ,  $\mathbf{x}_i = \mathbf{Q}\mathbf{x}_{b(i)} + \mathbf{t}$ . Notice that the condition requiring a rigid motion  $(\mathbf{Q}, \mathbf{t}) \in \text{E}(3)$

such that  $\mathbf{x}_i = \mathbf{Q}\mathbf{x}_{b(i)} + \mathbf{t}$  for all  $i$  is equivalent to the condition  $\|\mathbf{x}_i - \mathbf{x}_j\| = \|\mathbf{x}_{b(i)} - \mathbf{x}_{b(j)}\|$  for all  $i, j$ . A function  $F$  defined on the geometric graphs is said to be *invariant* if  $F(\mathcal{G}_1) = F(\mathcal{G}_2)$  for any two geometrically isomorphic geometric graphs  $\mathcal{G}_1, \mathcal{G}_2$ .

**Convex hull and polyhedral graph.** A *convex hull* of a set of points  $\{\mathbf{x}_1, \dots, \mathbf{x}_m\} \subset \mathbb{R}^3$  is defined as  $\text{Conv}(\{\mathbf{x}_1, \dots, \mathbf{x}_m\}) = \{\sum_i \alpha_i \mathbf{x}_i \mid \sum_i \alpha_i = 1, \alpha_1, \dots, \alpha_m \in [0, 1]\}$ , which is the smallest convex set containing these points. When the points are not coplanar, the convex hull is also known as a *convex polyhedron*, whose graph structure comprises its vertices, edges, and faces. Any graph derived from this structure is referred to as a *combinatorial polyhedron* or *polyhedral graph*. Steinitz’s Theorem (Grünbaum, 2007) establishes a one-to-one correspondence between polyhedral graphs and 3-connected simple planar graphs<sup>1</sup>. This means every polyhedral graph can be represented as a 3-connected simple planar graph and vice versa.

A *geometric polyhedral graph* is a geometric graph  $(\mathcal{V}, \mathcal{E}, \mathbf{X})$  whose underlying graph structure is a polyhedral graph. It can be considered as assigning node coordinates to a polyhedral graph  $(\mathcal{V}, \mathcal{E})$ . A well-known rigidity theorem for polyhedral graphs by Stoker (1968) (see also (Cho & Kim, 2023)) states that a strictly-convex geometric polyhedral graph is uniquely determined by its edge lengths  $d_{ij}$  and dihedral angle  $\tau_{ij}$  on edge  $(i, j)$ , where the dihedral angle on edge  $(i, j)$  is defined as the angle between two faces that contain edge  $(i, j)$ . More precisely, we have the following theorem:

**Theorem 2.1** (Stoker (1968)). *Let  $\mathcal{G} = (\mathcal{V}, \mathcal{E}, \mathbf{X})$  and  $\mathcal{G}' = (\mathcal{V}', \mathcal{E}', \mathbf{X}')$  be two strictly-convex geometric polyhedral graphs. Suppose there exists a graph isomorphism  $b : \mathcal{V} \rightarrow \mathcal{V}'$  satisfying  $\tau_{ij} = \tau'_{b(i)b(j)}$  and  $d_{ij} = d'_{b(i)b(j)}$  for any  $(i, j) \in \mathcal{E}$ , where  $d_{ij}$  and  $\tau_{ij}$  denote the length of edge  $(i, j) \in \mathcal{E}$  and dihedral angle associated with edge  $(i, j)$ . Then  $\mathcal{G}$  and  $\mathcal{G}'$  must be geometrically isomorphic, i.e., there is a rigid motion  $(\mathbf{Q}, \mathbf{t}) \in \mathbb{E}(3)$  such that  $\mathbf{x}_i = \mathbf{Q}\mathbf{x}'_{b(i)} + \mathbf{t}$  for any  $i \in \mathcal{V}$ .*

**Message-passing GNNs and their separation power.** For any geometric graph  $\mathcal{G} = (\mathcal{V}, \mathcal{E}, \mathbf{X}, \mathbf{F})$ , a message-passing GNN propagates features, with  $\mathbf{f}_i^{(0)} = \mathbf{f}_i$ , as follows:

$$\mathbf{f}_i^{(t+1)} = \text{UPD}(\mathbf{f}_i^{(t)}, \text{AGG}(\{\{\mathbf{f}_i^{(t)}, \mathbf{f}_j^{(t)}, e_{ij} \mid j \in \mathcal{N}_i\}\})), \quad (1)$$

where  $e_{ij}$  are edge attributes ( $e_{ij}$  can be  $\mathbf{x}_i - \mathbf{x}_j$  or pre-determined invariant edge attributes like relative distance  $\|\mathbf{x}_i - \mathbf{x}_j\|$ ),  $\mathcal{N}_i$  denotes the one-hop neighbors of node  $i$ , i.e., the set of nodes in  $\mathcal{V}$  that are reachable from  $i$  through an edge in  $\mathcal{E}$ , and UPD and AGG are learnable update and aggregate functions operating on the graph  $\mathcal{G}$ , respectively. After  $T$  message-passing steps, we apply a multiset Readout function to obtain the graph level global features

$$\mathbf{s}^{\text{global}} = \text{Readout}\left(\left\{\left\{\mathbf{f}_i^{(T)} \mid i \in \mathcal{V}\right\}\right\}\right). \quad (2)$$

A common approach to evaluating GNN’s performance is to assess its ability to learn distinct global features from non-isomorphic geometric graphs. In particular, a standard assumption in this analysis is to consider maximally expressive GNNs, where the update, aggregation, and readout functions are all injective (Joshi et al., 2023; Wang et al., 2024; Sverdlov & Dym, 2024). We say a maximally expressive GNN  $F$  with depth  $T$  can distinguish two geometric graphs  $\mathcal{G}_1$  and  $\mathcal{G}_2$  if, after  $T$  iterations, the learned global features for  $\mathcal{G}_1$  and  $\mathcal{G}_2$  are distinct, that is,  $\mathbf{s}_1^{\text{global}} =: F(\mathcal{G}_1) \neq F(\mathcal{G}_2) := \mathbf{s}_2^{\text{global}}$ .

### 3 MAIN RESULTS

In response to the limitation of existing graph representations – in achieving sparsity, connectivity, and rigidity – for geometric data with 3D coordinates, we propose SCHull – a new graph construction method for molecules and beyond. SCHull eliminates hyperparameter tuning and ensures connectivity while maintaining sparsity and rigidity. In this section, we will outline the two steps in constructing SCHull graphs, followed by proving how these steps achieve the desired properties and how the resulting graph benefits GNNs’ performance.

#### 3.1 SCHULL – A NEW GRAPH CONSTRUCTION

SCHull constructs graphs in two steps: (1) project points (nodes) onto the unit sphere centered at the center of the points, and (2) construct the convex hull for the projected points and connect two original points if the convex hull contains an edge connecting the two corresponding projected points.

<sup>1</sup>In this context, a simple graph is one without self-loops or multiple edges. A graph is 3-connected if removing fewer than three vertices doesn’t disconnect it. A graph is planar if it can be drawn on a plane without edge crossings.



**Step 1: Project points onto the unit sphere.** Let  $(\mathcal{V}, \mathbf{X} = [\mathbf{x}_1, \mathbf{x}_2, \dots, \mathbf{x}_m])$  be a point cloud, e.g., representing atoms in a protein molecule. Denote the center of  $\mathbf{X}$  by  $\bar{\mathbf{x}} := \frac{1}{m} \sum \mathbf{x}_i$ . Consider the projection  $p_{\bar{\mathbf{x}}} : \mathbb{R}^3 \rightarrow \mathbb{S}^2$  defined by  $\mathbf{x} \mapsto \frac{\mathbf{x} - \bar{\mathbf{x}}}{\|\mathbf{x} - \bar{\mathbf{x}}\|}$ , where  $\mathbb{S}^2 := \{\mathbf{x} \in \mathbb{R}^3 \mid \|\mathbf{x}\| = 1\}$  is the unit sphere. That is,  $p_{\bar{\mathbf{x}}}$  projects points onto the unit sphere centered at  $\bar{\mathbf{x}}$ . Applying this projection to all points, we obtain a new point cloud  $(\mathcal{V}, p_{\bar{\mathbf{x}}}(\mathbf{X}))$  on  $\mathbb{S}^2$ , where  $p_{\bar{\mathbf{x}}}(\mathbf{X}) = [p_{\bar{\mathbf{x}}}(\mathbf{x}_1), p_{\bar{\mathbf{x}}}(\mathbf{x}_2), \dots, p_{\bar{\mathbf{x}}}(\mathbf{x}_m)]$ .

In rare cases, there may be points such that  $\mathbf{x}_i = \bar{\mathbf{x}}$  for some  $i$ , which prevents us from defining its projection. To ease our analysis, we assume that the projections of all points in a given point cloud  $(\mathcal{V}, \mathbf{X})$  are well-defined and these projections on  $\mathbb{S}^2$  are distinct. This implies that  $|\mathcal{V}| = |\{p_{\bar{\mathbf{x}}}(\mathbf{x}_i) \mid i \in \mathcal{V}\}|$ . More precisely, we assume the following *generic condition* holds:

$$\mathbf{x}_i \neq \bar{\mathbf{x}} \text{ and } p_{\bar{\mathbf{x}}}(\mathbf{x}_i) \neq p_{\bar{\mathbf{x}}}(\mathbf{x}_j) \text{ for any } i \neq j \in \mathcal{V}. \tag{3}$$

Point clouds satisfy this condition with probability 1 if they are uniformly distributed; see Lemma 3.4. We focus on this case in the main context and present a strategy in Appendix D to maintain the desired properties of our graph when the generic condition equation (3) does not hold.

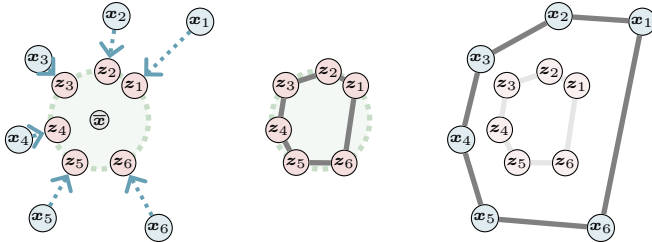


Figure 3: Visualizing the SCHull graph construction process: (left panel) The blue points  $\mathbf{x}_i$ s represent the given point cloud, and the gray node  $\bar{\mathbf{x}}$  denotes the center of this point cloud. Each point is projected onto the green unit sphere centered at  $\bar{\mathbf{x}}$ , resulting in the corresponding orange points  $\mathbf{z}_i = p_{\bar{\mathbf{x}}}(\mathbf{x}_i)$ . (middle panel) The convex hull of the orange points  $\mathbf{z}_i = p_{\bar{\mathbf{x}}}(\mathbf{x}_i)$  is constructed, with its edges highlighted in gray. (right panel) The gray edges on the convex hull of the projected points induce the graph structure on the original point cloud.

**Step 2: Construct the convex hull and SCHull graph.** Next, we construct a convex hull – using the QuickHull algorithm (Barber et al., 1996) – for the projected points  $(\mathcal{V}, p_{\bar{\mathbf{x}}}(\mathbf{X}))$  obtained from Step 1, and we denote the resulting convex hull as  $\text{Conv}(\{p_{\bar{\mathbf{x}}}(\mathbf{x}_i) \mid i \in \mathcal{V}\})$ . In particular, the boundary of this convex hull is a polyhedral graph with nodes, edges, and faces. By disregarding the face structure, we obtain a graph  $(\mathcal{V}, \mathcal{E})$  that includes all points in  $\mathcal{V}$  thanks to the generic condition equation (3). Our graph construction for the given point cloud  $(\mathcal{V}, \mathbf{X})$  is then defined as  $\mathcal{G} = (\mathcal{V}, \mathcal{E}, \mathbf{X})$ . This graph includes the original point cloud  $(\mathcal{V}, \mathbf{X})$ , with edges defined by those on the convex hull of  $(\mathcal{V}, p_{\bar{\mathbf{x}}}(\mathbf{X}))$ . Specifically, nodes  $i, j$  are connected by an edge in  $\mathcal{E}$  if and only if their projected points on the unit sphere  $p_{\bar{\mathbf{x}}}(\mathbf{x}_i), p_{\bar{\mathbf{x}}}(\mathbf{x}_j)$  are connected by an edge on the convex hull  $\text{Conv}(\{p_{\bar{\mathbf{x}}}(\mathbf{x}_i) \mid i \in \mathcal{V}\})$ .

We demonstrate an example of applying our SCHull graph construction for a synthetic point cloud in Fig. 3. For simplicity, we assume all points  $\{\mathbf{x}_i\}_{i=1}^6$  are coplanar. The green circle represents the unit sphere centered at the mean point  $\bar{\mathbf{x}} = \frac{1}{6} \sum_{i=1}^6 \mathbf{x}_i$ . Each  $\mathbf{z}_i := p_{\bar{\mathbf{x}}}(\mathbf{x}_i)$  denotes the projection of  $\mathbf{x}_i$  onto the green unit sphere. We then construct the convex hull  $\text{Conv}(\{\mathbf{z}_i\})$  of the projected points, with solid gray lines indicating the edges. Finally, the SCHull graph is created by connecting points  $\mathbf{x}_i$  and  $\mathbf{x}_j$  if their corresponding projections  $\mathbf{z}_i$  and  $\mathbf{z}_j$  are connected by an edge in the convex hull.

**Computational complexity.** To analyze the computational complexity of constructing SCHull graphs, let  $m$  be the number of points in the point cloud. The overall cost is dominated by the convex hull construction, which utilizes QuickHull with a computational complexity of  $\mathcal{O}(m \log m)$  (Barber et al., 1996). Other steps, including projecting points to the unit sphere and attributes computation (see Section 3.3), resulting in  $\mathcal{O}(m)$  additional computational complexity.

### 3.2 CONNECTIVITY AND SPARSITY OF SCHULL GRAPHS

In this section, we prove that SCHull graphs are connected and sparse. We begin by presenting a fundamental proposition that outlines the properties of convex hulls formed by points on a sphere.

**Proposition 3.1.** *Let  $\mathcal{Z} = \{\mathbf{z}_j\}$  be a set of points on a sphere where  $|\mathcal{Z}| \geq 3$  (the number of points is at least 3), and let  $\text{Conv}(\mathcal{Z})$  denote the convex hull of  $\mathcal{Z}$  with its associated graph structure consisting of nodes, edges, and faces defined by its boundary. Then, we have*

1. *Connectivity*: Any two points in  $\mathcal{Z}$  are connected by a sequence of edges in  $\text{Conv}(\mathcal{Z})$ .
2. *Sparsity*: The number of edges in  $\text{Conv}(\mathcal{Z})$  is no greater than  $3|\mathcal{Z}| - 6$ .

Moreover,  $\text{Conv}(\mathcal{Z})$  is a strictly convex geometric polyhedral graph if  $z_j$ s are not coplanar.

Proposition 3.1 ensures that the convex hull of a finite set of points on a sphere is always connected, eliminating the possibility of isolated points. Additionally, the number of edges is bounded above by three times the number of nodes, ensuring sparsity. Notice the SCHull graph directly inherits the graph structure from the convex hull of the projected points on the unit sphere, along with its connectivity and sparsity. We summarize these implications in the following corollary:

**Corollary 3.2.** *For any point cloud  $(\mathcal{V}, \mathbf{X})$  with more than 2 points and satisfying the generic condition equation (3), the SCHull graph  $(\mathcal{V}, \mathcal{E}, \mathbf{X})$  is a connected geometric polyhedral graph and has a linear relationship between the number of edges and the number of nodes. Specifically, the edge-to-node ratio is bounded above by 3, i.e.  $\frac{|\mathcal{E}|}{|\mathcal{V}|} < 3$ .*

The theoretical results in Corollary 3.2 are numerically substantiated by the results in Fig. 1. In particular, SCHull graphs are always connected, and the ratios between the number of edges and the number of nodes are always bounded above by 3 for all molecules in the benchmark Fold dataset.

### 3.3 RIGIDITY OF SCHULL GRAPHS AND ITS ROLE IN GNN’S PERFORMANCE

SCHull graphs guarantee both sparsity and connectivity. However, a crucial question remains:

*How do SCHull graphs impact the performance of GNNs?*

To answer this affirmatively, we delve into the rigidity of SCHull graphs. We first introduce a common assumption about the genericity of point clouds in graph rigidity studies; see e.g., (Laman, 1970; Asimow & Roth, 1978; Connelly, 2005). We then propose a simple attribute-based design for SCHull graphs and provide a theoretical analysis demonstrating that our SCHull graphs – with their geometric attributes on both edges and nodes – can effectively enable GNNs to distinguish between any two non-isomorphic generic point clouds.

**Definition 3.3** (Genericity of point clouds). A point cloud  $(\mathcal{V}, \mathbf{X})$  is said to be *generic*<sup>2</sup> if

$$\text{No multivariate polynomial } P \text{ with rational coefficients satisfies } P(\mathbf{x}_1, \dots, \mathbf{x}_m) = 0. \quad (4)$$

The genericity of a point cloud means that the points are arranged in a way that cannot be described by a simple polynomial equation with rational coefficients. It’s important to note that almost all point clouds are generic, with exceptions forming a set of Lebesgue measure zero (Mityagin, 2015). In particular, the genericity of point clouds presented in Definition 3.3 is stronger than the generic condition equation (3) that we have assumed in Section 3.1.

**Lemma 3.4.** *Any generic point cloud satisfies the generic assumption equation (3).*

Moreover, generic point clouds also avoid the cases where all the projected points  $\{p_{\bar{\mathbf{x}}}(\mathbf{x}_i)\}$  are coplanar; this leads to the following result, allowing us to apply Theorem 2.1.

**Lemma 3.5.** *Let  $(\mathcal{V}, \mathbf{X})$  be a generic point cloud. Then  $\text{Conv}(\{p_{\bar{\mathbf{x}}}(\mathbf{x}_i) \mid i \in \mathcal{V}\})$  – the convex hull on the sphere we constructed in Section 3.1 – is a strictly convex geometric polyhedral graph.*

According to Lemma 3.5 and Theorem 2.1, edge lengths  $d_{ij}$  and dihedral angles  $\tau_{ij}$  are sufficient to uniquely determine the spatial arrangement of  $\text{Conv}(\{p_{\bar{\mathbf{x}}}(\mathbf{x}_i) \mid i \in \mathcal{V}\})$  due to its convexity. While the SCHull graph is also a geometric polyhedral graph, its lack of convexity raises concerns about whether edge lengths and dihedral angles are sufficient to determine the spatial arrangement of points.

However, by including the original distances of the nodes from the center of the point clouds as node attributes, we can prove that any maximally expressive GNN – a standard framework for analyzing GNNs’ performance – can distinguish between any two non-isomorphic point clouds (see Section 2 for a brief overview). Specifically, for a given point cloud  $(\mathcal{V}, \mathbf{X})$ , we consider the attributed version of our SCHull graph  $\mathcal{G} = (\mathcal{V}, \mathcal{E}, \mathbf{X}, \mathbf{F})$ , where we encode

$$\begin{aligned} &\text{the edge attributes } e_{ij} = (\|\mathbf{x}_i - \mathbf{x}_j\|, \tau_{ij}) \text{ for any } (i, j) \in \mathcal{E}, \text{ and} \\ &\text{the node attributes } f_i = \|\mathbf{x}_i - \bar{\mathbf{x}}\| \text{ for any } i \in \mathcal{V}. \end{aligned} \quad (5)$$

<sup>2</sup>Also known as algebraically independent.

Notice that  $\tau_{ij}$  are the dihedral angles between faces computed on  $\text{Conv}(\{p_{\bar{x}}(\mathbf{x}_i) \mid i \in \mathcal{V}\})$ . Under these settings, we have

**Theorem 3.6.** *Let  $F$  be a maximally expressive GNN with depth  $T = 1$ . Then  $F$  can distinguish between the attributed SCHull graphs defined in equation (5) of any two non-isomorphic generic point clouds.*

*Remark 3.7.* The node attribute design of SCHull in equation (5) can be omitted without affecting the theorem’s result if we consider removing an additional measure zero subset of point clouds. Due to page limitations, this version of Theorem 3.6 is provided in Appendix F. **Additionally, while we do not address the coplanar case in the main text, the corresponding theory and discussion regarding the effectiveness of our SCHull graph for coplanar cases can be found in Appendix E.**

*Remark 3.8.* As discussed in the introduction, the rigidity property does not generally hold for other graph construction methods, e.g., radial cutoff. While Sverdllov & Dym (2024) propose power graphs as a solution to ensure rigidity in these methods, power graphs often lead to increased graph density and do not address cases where the original graph is disconnected. **A more detailed introduction of power graphs is provided in Appendix A and an empirical study is provided in Appendix B.** In contrast, the SCHull graph – when dealing with generic point clouds – naturally strikes a balance between rigidity and sparsity, making it an efficient and suitable option for GNN applications.

*Remark 3.9.* Existing works, such as (Joshi et al., 2023; Li et al., 2024; Hordan et al., 2024), have established theoretical frameworks that address both generic and non-generic point clouds. In particular, Li et al. (2024) highlights the challenges of distinguishing ambiguous symmetric point clouds. While our method does not currently provide a theoretical guarantee for such cases, we present empirical evidence in Appendix B showing that even shallow graph neural networks using our approach can effectively distinguish ambiguous symmetric point clouds – cases where incorporating all edge lengths on complete graphs fall short.

To solidify Theorem 3.6, we design a synthetic dataset named NestedSquares. The NestedSquares dataset comprises ten graphs, each consisting of two nested squares. In each graph, the inner square is rotated by an angle  $\theta \in (0, \pi/2)$ ; see Fig. 4 for an example. Each graph is labeled with the angular rotation, and the objective is to minimize the mean squared error when predicting this angle. The data is split into 6 training graphs, 2 test graphs, and 2 validation graphs. This task evaluates GNNs’ ability to learn both local and global geometric information. To show the effectiveness of SCHull graphs, we compare message passing using solely the information provided by SCHull against existing geometric GNNs with common graph constructions. We introduce MPNN+SCHull, a message-passing neural network (MPNN) that takes the SCHull graph as input, incorporating both graph structure and the constructed edge attributes and node features as defined in equation (5); see Appendix G.2 for the detailed architecture of the used MPNN, and Appendix H.1 for experimental details.

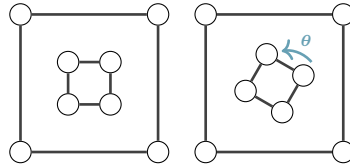


Figure 4: Depicting the rotation of the graph from the NestedSquares dataset. Ten rotated graphs are generated by randomly choosing  $\theta$ .

	Radial cutoff	$k$ NN ( $k = 3$ )	Voronoi	SCHull (ours)
MPNN	$0.657 \pm 0.165$	$0.213 \pm 0.013$	$0.281 \pm 0.049$	<b><math>0.068 \pm 0.049</math></b>
DimeNet++	$0.281 \pm 0.049$	$0.281 \pm 0.049$	$0.292 \pm 0.018$	—
SphereNet	$0.661 \pm 0.212$	$0.450 \pm 0.121$	$0.494 \pm 0.128$	—
ComENet	$0.885 \pm 0.287$	$0.502 \pm 0.1928$	$0.816 \pm 0.275$	—

Table 2: Test mean squared error (MSE) of single layer invariant GNNs for the NestedShapes dataset. MPNN+SCHull utilizes the SCHull graph structure. Our method outperforms all other models and graph constructions. The mean  $\pm$  standard deviation is reported from 10 random trials.

In particular, we cover several representative invariant GNN models, including DimeNet++ (Gasteiger et al., 2020a), SphereNet (Liu et al., 2022), and ComENet (Wang et al., 2022b). These invariant GNNs, along with the simple MPNN, were equipped with various graphs, including Radial cutoff,  $k$ NN, and Voronoi. Notably, we did not implement other invariant GNNs on SCHull to avoid any potential biases introduced by their specific designs. Table 2 shows the advantage of SCHull over other graphs with different invariant GNN models. Notice that MPNN+SCHull significantly outperforms all other models almost by an order of magnitude.

### 3.4 SOME FURTHER DISCUSSIONS

While SCHull graphs have connectivity, sparsity, and rigidity guarantees, their performance in practice may vary depending on the complexity of the problem. Our proposed SCHull graph is more likely to connect distant nodes, capturing global information but potentially overlooking local details. To fully leverage the strengths of SCHull graphs, we recommend using them in conjunction with an additional informative sparse graph, such as a radial cutoff graph with a small cutoff threshold or a chemical graph. This combined approach can ensure both global geometric completeness and capture of local information while maintaining connectivity and sparsity.

To demonstrate the integration of SCHull graphs with existing GNNs that use radial cutoff graphs, we consider a geometric graph  $\mathcal{G} = (\mathcal{V}, \mathcal{E}, \mathbf{X}, \mathbf{F})$  constructed using the radial cutoff method from the point cloud  $(\mathcal{V}, \mathbf{X})$ . We then construct the corresponding SCHull graph  $\tilde{\mathcal{G}} = (\mathcal{V}, \tilde{\mathcal{E}}, \mathbf{X}, \tilde{\mathbf{F}})$ . Notice that most GNNs – e.g., (Wang et al., 2022a; Liu et al., 2022; Jing et al., 2020) – utilize a predefined embedding function  $\text{EMB}(\mathcal{E}, \mathbf{X}, \mathbf{F})$ , to obtain the edge attributes  $e = \{e_{ij} \mid (i, j) \in \mathcal{E}\}$  and the embedded node features  $\mathbf{F}' = [\mathbf{f}'_1, \dots, \mathbf{f}'_m]$  on the graph  $\mathcal{G}$ . These attributed graphs are then input to the GNN model. We apply the same embedding function to compute the edge attributes  $\tilde{e} = \{\tilde{e}_{ij} \mid (i, j) \in \tilde{\mathcal{E}}\}$  and the embedded node features  $\tilde{\mathbf{F}}' = [\tilde{\mathbf{f}}'_1, \dots, \tilde{\mathbf{f}}'_m]$  for the SCHull graph  $\tilde{\mathcal{G}}$ . It is worth mentioning that the embedded features  $\tilde{e}$  and  $\tilde{\mathbf{F}}'$  contain the features mentioned in equation (5). We then define the integrated node features as  $\mathbf{F}^* = \mathbf{F}' \oplus \tilde{\mathbf{F}}'$ , and the integrated edges and edge attributes as  $\mathcal{E}^* = \mathcal{E} \cup \tilde{\mathcal{E}}$  and  $e^* = e \cup \tilde{e}$ , respectively. Finally, we obtain the SCHull integrated graph  $\mathcal{G}^* = (\mathcal{V}, \mathcal{E}^*, \mathbf{X}, \mathbf{F}^*)$ , which serves as the input to the GNNs.

## 4 NUMERICAL RESULTS

We present comprehensive empirical results to show the effectiveness of SCHull-integrated GNNs. Across various tasks, we highlight that: (1) The SCHull graph’s connectivity and sparsity properties effectively capture geometric information while maintaining computational efficiency. (2) The enriched graph structure, coupled with comprehensive node and edge features, significantly enhances message-passing capabilities. To validate our approach, we integrate SCHull into several GNN models and evaluate their performance on both small- and large-scale graph tasks, including atom force prediction, protein fold and enzyme reaction classification, and protein property prediction. The results consistently demonstrate that SCHull-integrated GNN models outperform the baseline models across multiple metrics, while maintaining computational efficiency.

**Software and equipment:** Our implementation relies on the PyTorch Geometric (Fey & Lenssen, 2019) and SciPy (Virtanen et al., 2020) frameworks. Experiments are conducted on a single NVIDIA RTX 3090 GPU, and T4 and A100 GPUs provided by Google Colab (Google Colaboratory, 2023).

**Training setup:** The training setups for different tasks are available in Appendices I.2 and I.3.

**Datasets and models:** We integrate SCHull graphs into DimeNet (Gasteiger et al., 2020b), SphereNet (Liu et al., 2022) and LEFTNet (Du et al., 2024) for learning node-level equivariant features on molecule dataset MD17 (Chmiela et al., 2017). Also, we integrate SCHull into ProNet-Backbone, ProNet-Amino-Acid (Wang et al., 2022a), and GVP-GNN (Jing et al., 2020) for benchmark tasks of protein fold classification (Fold) and enzyme reaction classification (React) (Hou et al., 2018), and protein-ligand binding affinity prediction (LBA) (Wang et al., 2004; Liu et al., 2015).

**Metrics:** For prediction, we use various metrics depending on the tasks e.g., mean absolute error (MAE), root mean square error (RMSE), Pearson Correlation (Uebersax, 1987), Spearman Correlation (Panda & Pati, 2015) and Kendall Correlation (Bradley, 1976). For each task, we run the experiment five times and record the standard deviation of the corresponding metric.

### 4.1 PREDICTING ATOMIC FORCES FOR MD17 SMALL MOLECULES

In this experiment, we evaluate how effectively the SCHull framework enhances different models in learning equivariant features by predicting atomic forces on the MD17 dataset. We integrate SCHull into LEFTNet, DimeNet, and SphereNet. Following prior research (Schütt et al., 2018; Liu et al., 2022; Du et al., 2024), we train individual models for each of the seven molecules: Aspirin, Benzene, Ethanol, Malonaldehyde, Naphthalene, Toluene, and Uracil. Detailed experimental and hyperparameter settings are provided in Appendices H.2 and I.2, respectively. Both the training and validation sets consist of 1,000 samples each, with the remaining data reserved for testing.

We use MAE to assess model performance on the test dataset. The results in Table 3 show that all SCHull-integrated models outperform baselines on MD17 while maintaining comparable runtime. This indicates that SCHull enhances the models’ ability to capture equivariant information without significantly affecting message-passing efficiency.

Molecule	DimeNet	DimeNet+SCHull	SphereNet	SphereNet+SCHull	LEFTNet	LEFTNet+SCHull
Aspirin	0.499	0.427 $\pm$ .004	0.430	0.387 $\pm$ .005	0.281	<b>0.240</b> $\pm$ .005
Benzene	0.187	0.157 $\pm$ .006	0.178	0.155 $\pm$ .004	0.147	<b>0.098</b> $\pm$ .002
Ethanol	0.230	0.198 $\pm$ .003	0.208	0.181 $\pm$ .003	0.138	<b>0.109</b> $\pm$ .002
Malonaldehyde	0.383	0.334 $\pm$ .003	0.340	0.298 $\pm$ .003	0.205	<b>0.151</b> $\pm$ .002
Naphthalene	0.215	0.178 $\pm$ .002	0.178	0.144 $\pm$ .002	0.074	<b>0.058</b> $\pm$ .001
Toluene	0.210	0.169 $\pm$ .002	0.155	0.129 $\pm$ .002	0.083	<b>0.076</b> $\pm$ .001
Uracil	0.301	0.288 $\pm$ .002	0.267	0.242 $\pm$ .003	0.117	<b>0.095</b> $\pm$ .001
Training Time/Epoch(s)	43 $\pm$ 0.9	50 $\pm$ 0.8	51 $\pm$ 1.0	62 $\pm$ 1.5	24 $\pm$ 0.5	28 $\pm$ 0.5

Table 3: Test MAEs of MD17 dataset vector-valued properties prediction.

## 4.2 LEARNING LARGE PROTEIN MOLECULES

We demonstrate the importance of ensuring connectivity and sparsity in large-scale graph tasks, such as protein classification and property prediction. Protein graphs can contain thousands of nodes, making it crucial to maintain graph sparsity for computational efficiency while preserving connectivity to allow GNNs to capture global geometric information. We integrate SCHull into protein-task-specific GNNs – such as ProNet-Backbone, ProNet-Amino-Acid, GVP-GNN, [SEGNN](#), and [MACE](#) – and evaluate them on three protein datasets. Details of the model training and hyperparameters are provided in Appendix I.3. The experimental results highlight the significance of capturing global information during message passing using SCHull features, particularly in large graphs. Additionally, including SCHull does not introduce significant overhead in terms of runtime.

### 4.2.1 FOLD CLASSIFICATION

Protein fold classification (Levitt & Chothia, 1976) informs the connection between protein structure and function, as well as protein evolution. In this experiment, we assess our SCHull integrated models for the protein fold classification task by following the fold dataset and experimental frameworks in (Wang et al., 2022a). To evaluate generalization performance, three test sets are used:

- **Family:** includes proteins from the same family in the training data.
- **Superfamily:** excludes proteins from the same family appearing in the training data.
- **Fold:** excludes proteins from the same superfamily appearing in the training data.

More dataset information and splits can be found in Appendix H.3. Table 4 demonstrates that SCHull improves model accuracy across all three test datasets, with only a marginal increase in runtime. Furthermore, to assess how SCHull aids models in capturing global information, we divide each test set into four subsets based on the number of nodes (with at most 150, 300, 450, and 600 nodes). Fig. 5 shows that as graph size increases, the SCHull-integrated ProNet-Backbone achieve progressively higher accuracy over its original model. This result supports our claim that preserving connectivity is crucial for GNNs to learn global information and predict the class of protein data. Indeed, our proposed SCHull graph ensures connectivity, as shown in Fig. 1.

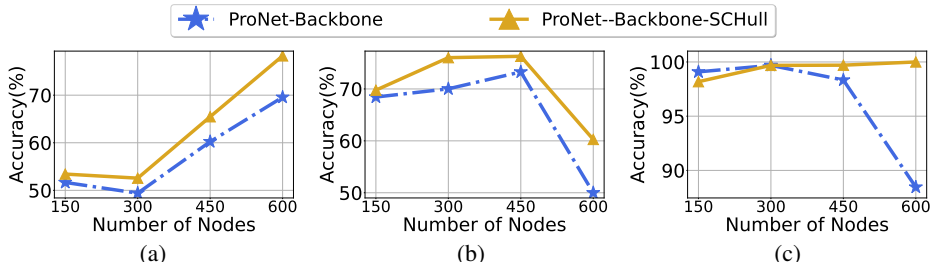


Figure 5: Comparison of the accuracy (%) on different size of graphs in Fold classification dataset using ProNet(Backbone) and ProNet(Backbone)+SCHull. (a) Accuracy on test(Fold) dataset; (b) Accuracy on test(Super) dataset; (c) Accuracy on test(Family) dataset with at most 150, 300, 450, and 600 nodes.

### 4.2.2 REACTION CLASSIFICATION

Enzymes are proteins functioning as biological catalysts. They can be categorized using enzyme commission (EC) numbers which classify enzymes according to the reactions they facilitate (Omelchenko

Method	React	Ave. Time	Fold				Avg. Time
			Fold	Super	Family	Avg.	
GCN (Kipf & Welling, 2017)	67.3	–	16.8	21.3	82.8	40.3	–
IEConv (Hermosilla et al., 2020)	87.2	–	45.0	69.7	98.9	71.2	–
DWNN (Li, 2022)	76.7	–	31.8	37.8	85.2	51.5	–
GearNet (Zhang et al., 2022)	79.4	–	28.4	42.6	95.3	55.4	–
HoloProt (Somnath et al., 2021)	78.9	–	–	–	–	–	–
MACE (Batatia et al., 2022)	–	–	23.7 $\pm$ 0.5	21.4 $\pm$ 0.5	60.2 $\pm$ 0.2	35.1	114 $\pm$ 0.5
MACE+SCHull	–	–	27.0 $\pm$ 0.6	23.1 $\pm$ 0.5	65.0 $\pm$ 0.2	38.4	135 $\pm$ 0.5
SEGNN (Brandstetter et al.)	–	–	28.8 $\pm$ 0.6	30.3 $\pm$ 0.6	77.1 $\pm$ 0.3	45.4	121 $\pm$ 0.7
SEGNN+SCHull	–	–	32.0 $\pm$ 0.4	36.8 $\pm$ 0.7	86.9 $\pm$ 0.3	51.9	152 $\pm$ 0.5
GVP-GNN (Jing et al., 2020)	65.5	320 $\pm$ 5	16.0	22.5	83.8	40.8	106.3 $\pm$ 0.5
GVP-GNN + SCHull	77.1 $\pm$ 0.5	345 $\pm$ 5	24.5 $\pm$ 0.3	27.1 $\pm$ 0.2	88.6 $\pm$ 0.3	46.7	111.5 $\pm$ 0.5
ProNet-Amino-Acid (Wang et al., 2022a)	86.0	210 $\pm$ 5	51.5	69.9	99.0	73.5	70.5 $\pm$ 0.5
ProNet-Amino Acid+SCHull	87.9 $\pm$ 0.3	221 $\pm$ 6	55.2 $\pm$ 0.2	73.9 $\pm$ 0.2	99.1 $\pm$ 0.1	76.1	73.8 $\pm$ 0.5
ProNet-Backbone (Wang et al., 2022a)	86.4	213 $\pm$ 5	52.7	70.3	99.3	74.1	71.4 $\pm$ 0.8
ProNet-Backbone+SCHull	<b>88.1</b> $\pm$ 0.3	230 $\pm$ 5	<b>56.1</b> $\pm$ 0.3	<b>74.6</b> $\pm$ 0.2	<b>99.4</b> $\pm$ 0.1	<b>76.7</b>	75.8 $\pm$ 0.5

Table 4: Accuracy (%) on protein fold and enzyme reaction classification tasks. **Ave. Time** denotes the average time per training epoch. The top results are in boldface. SCHull consistently improves baseline models.

et al., 2010). In this experiment, we evaluate the SCHull-integrated models on the reaction classification task using the same reaction dataset and experimental settings as outlined in (Wang et al., 2022a; Hou et al., 2018). Additional details on the dataset and the training, validation, and test splits are provided in Appendix H.3. Similar to the fold classification results in Section 4.2.1, Table 4 shows that SCHull consistently outperforms the original models, with a minimal increase in runtime.

#### 4.2.3 LIGAND BINDING AFFINITY

Predicting protein-ligand binding affinity (LBA) plays a crucial role in various downstream processes in drug discovery. For this task, we use the SCHull-integrated models to predict LBA. The dataset is sourced from PDBbind (Wang et al., 2004; Liu et al., 2015) along with the experimental protocols established by (Jing et al., 2020). We employ default dataset split. See Appendix H.3 for more details of the dataset. We use a variety of statistical metrics, including RMSE, Pearson, Spearman, and Kendall correlations, to evaluate how SCHull enhances the learning capacity and generalization of GNNs. Again, Table 5 shows that SCHull-integrated models consistently outperform the original models across different metrics while maintaining high computational efficiency.

Method	LBA				Avg. Time
	RMSE $\downarrow$	Pearson $\uparrow$	Spearman $\uparrow$	Kendall $\uparrow$	
IEConv (Hermosilla et al., 2020)	1.554	0.414	0.428	–	–
HoloProt-Full Surface (Somnath et al., 2021)	1.464	0.509	0.500	–	–
HoloProt-Superpixel (Somnath et al., 2021)	1.491	0.491	0.482	–	–
GVP-GNN (Jing et al., 2020)	1.529 $\pm$ 0.001	0.441 $\pm$ 0.001	0.432 $\pm$ 0.002	0.301 $\pm$ 0.002	48.6 $\pm$ 0.6
GVP-GNN + SCHull	1.401 $\pm$ 0.001	0.475 $\pm$ 0.001	0.459 $\pm$ 0.001	0.335 $\pm$ 0.002	53.6 $\pm$ 0.6
ProNet-Amino-Acid (Wang et al., 2022a)	1.455	0.536	0.526	0.465 $\pm$ 0.001	31.7 $\pm$ 0.5
ProNet-Amino Acid+SCHull	1.355 $\pm$ 0.002	0.556 $\pm$ 0.001	0.568 $\pm$ 0.001	0.512 $\pm$ 0.001	33.9 $\pm$ 0.5
ProNet-Backbone (Wang et al., 2022a)	1.458	0.546	0.550	0.481 $\pm$ 0.001	32.1 $\pm$ 0.5
ProNet-Backbone+SCHull	<b>1.321</b> $\pm$ 0.002	<b>0.581</b> $\pm$ 0.001	<b>0.578</b> $\pm$ 0.1	<b>0.535</b> $\pm$ 0.001	34.4 $\pm$ 0.5

Table 5: RMSE/Pearson Correlation/Spearman Correlation/Kendall Correlation on the LBA Test Dataset. **Ave. Time** refers to the average running time of one epoch in model training.

## 5 CONCLUDING REMARKS

In this paper, we introduce SCHull – a new computationally efficient and scalable method for constructing graph representations of molecules, large proteins, and general data with 3D point clouds. The SCHull graphs are guaranteed to be sparse, connected, and rigid; these properties are essential for learning biomolecules using graph neural networks. Furthermore, our proposed SCHull graph can be seamlessly integrated into the existing learning framework to boost the performance of existing models. There are a few avenues for future work. One particular question is if the rigidity, sparsity, and connected properties of the proposed SCHull graphs help solve global positioning problems from partial distance information (Biswas et al., 2006; Singer & Cucuringu, 2010). **Another important avenue is investigating whether the SCHull graph can ensure the maximal expressive power of GNNs for distinguishing non-generic point clouds, as demonstrated in the experiments in Appendix B.**



## 6 ETHICS STATEMENT

In this paper, we propose a new graph representation for geometric data with 3D coordinates, especially molecules. The new graph solves some fundamental challenges of existing graph representations for molecules. In particular, existing graphs struggle to ensure sparsity, connectivity, and rigidity. These merits are essential for the success of machine learning for molecular modeling. Our work belongs to fundamental research and are expect to improve existing models for learning geometric data. Our work is methodological, and we validate our proposed approaches on the benchmark datasets. We do not expect to cause negative societal problems. Furthermore, we do not see any issues with potential conflicts of interest and sponsorship, discrimination/bias/fairness concerns, privacy and security issues, legal compliance, and research integrity issues (e.g., IRB, documentation, research ethics).

## 7 REPRODUCIBILITY STATEMENT

We are committed to conducting reproducible research. To ensure the integrity and transparency of our work, we employ a multifaceted approach: First, we meticulously compare the novelty of our research against existing literature. This involves a thorough examination of the current state of the field to identify gaps in knowledge and demonstrate the unique contributions of our work. Second, we provide detailed derivations of our proposed approaches and theoretical results. By carefully outlining the mathematical underpinnings of our methods, we enhance the understanding of our work and facilitate its verification by others. Third, we conduct rigorous experiments using widely recognized benchmark datasets. This allows us to evaluate the performance of our methods against established standards and provides a solid foundation for comparison with other approaches. Fourth, we meticulously report experimental details, including the specific datasets used, parameters chosen, and evaluation metrics employed. Finally, we make all experimental codes, accompanied by comprehensive documentation, publicly available. This open-source approach empowers researchers to inspect our methods, verify our results, and build upon our work. By sharing our code, we foster collaboration, advance the field, and contribute to the overall reproducibility of scientific research.

## REFERENCES

- Leonard Asimow and Ben Roth. The rigidity of graphs. *Transactions of the American Mathematical Society*, 245:279–289, 1978.
- C. Bradford Barber, David P. Dobkin, and Hannu Huhdanpaa. The quickhull algorithm for convex hulls. *ACM Trans. Math. Softw.*, 22(4):469–483, dec 1996. ISSN 0098-3500. doi: 10.1145/235815.235821. URL <https://doi.org/10.1145/235815.235821>.
- Ilyes Batatia, Dávid Péter Kovács, Gregor NC Simm, Christoph Ortner, and Gábor Csányi. Mace: Higher order equivariant message passing neural networks for fast and accurate force fields. *arXiv preprint arXiv:2206.07697*, 2022.
- Claudio Battiloro, Ege Karaismailoğlu, Mauricio Tec, George Dasoulas, Michelle Audirac, and Francesca Dominici. E (n) equivariant topological neural networks. *arXiv preprint arXiv:2405.15429*, 2024.
- Helen M Berman, John Westbrook, Zukang Feng, Gary Gilliland, Talapady N Bhat, Helge Weissig, Ilya N Shindyalov, and Philip E Bourne. The protein data bank. *Nucleic acids research*, 28(1): 235–242, 2000.
- Pratik Biswas, Tzu-Chen Lian, Ta-Chung Wang, and Yinyu Ye. Semidefinite programming based algorithms for sensor network localization. *ACM Transactions on Sensor Networks (TOSN)*, 2(2): 188–220, 2006.
- Ralph Allan Bradley. Kendall’s tau and spearman’s rank correlation coefficient in the context of the theory of probabilistic dependence. *Biometrika*, 63(3):403–414, 1976. doi: 10.2307/2335758.
- Johannes Brandstetter, Rob Hesselink, Elise van der Pol, Erik J Bekkers, and Max Welling. Geometric and physical quantities improve e (3) equivariant message passing, 2021. URL <https://arxiv.org/abs/2110.02905>.

- 594 Serena H. Chen and David R. Bell. Evolution of thyroglobulin loop kinetics in epcam. *Life*, 11  
595 (9), 2021. ISSN 2075-1729. doi: 10.3390/life11090915. URL [https://www.mdpi.com/  
596 2075-1729/11/9/915](https://www.mdpi.com/2075-1729/11/9/915).  
597
- 598 Serena H. Chen, M. Todd Young, John Gounley, Christopher Stanley, and Debsindhu Bhowmik.  
599 How distinct structural flexibility within sars-cov-2 spike protein reveals potential therapeutic  
600 targets. In *2021 IEEE International Conference on Big Data (Big Data)*, pp. 4333–4341, 2021.  
601 doi: 10.1109/BigData52589.2021.9671323.
- 602 Shiing Shen Chern. Curves and surfaces in euclidean space. *Studies in global geometry and analysis*,  
603 4(1):967, 1967.  
604
- 605 Stefan Chmiela, Alexandre Tkatchenko, Huziel E Saucedo, Igor Poltavsky, Kristof T Schütt, and  
606 Klaus-Robert Müller. Machine learning of accurate energy-conserving molecular force fields.  
607 *Science advances*, 3(5):e1603015, 2017.
- 608 Yunhi Cho and Seonhwa Kim. Rigidity of nonconvex polyhedra with respect to edge lengths and  
609 dihedral angles. *arXiv preprint arXiv:2307.14769*, 2023.  
610
- 611 Robert Connelly. Generic global rigidity. *Discrete & Computational Geometry*, 33:549–563, 2005.  
612
- 613 Jose M Dana, Aleksandras Gutmanas, Nidhi Tyagi, Guoying Qi, Claire O’Donovan, Maria Martin,  
614 and Sameer Velankar. Sifts: updated structure integration with function, taxonomy and sequences  
615 resource allows 40-fold increase in coverage of structure-based annotations for proteins. *Nucleic  
616 acids research*, 47(D1):D482–D489, 2019.
- 617 Yuanqi Du, Limei Wang, Dieqiao Feng, Guifeng Wang, Shuiwang Ji, Carla P Gomes, Zhi-Ming Ma,  
618 et al. A new perspective on building efficient and expressive 3d equivariant graph neural networks.  
619 *Advances in Neural Information Processing Systems*, 36, 2024.
- 620 David K. Duvenaud, Dougal Maclaurin, Jorge Iparraguirre, Rafael Bombarell, Timothy Hirzel, Alán  
621 Aspuru-Guzik, and Ryan P Adams. Convolutional networks on graphs for learning molecular  
622 fingerprints. *Advances in neural information processing systems*, 2015.  
623
- 624 Floor Eijkelboom, Rob Hesselink, and Erik J Bekkers. E ( $n$ ) equivariant message passing simplicial  
625 networks. In *International Conference on Machine Learning*, pp. 9071–9081. PMLR, 2023.
- 626 Matthias Fey and Jan E. Lenssen. Fast graph representation learning with PyTorch Geometric. In  
627 *ICLR Workshop on Representation Learning on Graphs and Manifolds*, 2019.  
628
- 629 Patrick J Fleming and Karen G Fleming. Hullrad: fast calculations of folded and disordered protein  
630 and nucleic acid hydrodynamic properties. *Biophysical journal*, 114(4):856–869, 2018.
- 631 Johannes Gasteiger, Shankari Giri, Johannes T. Margraf, and Stephan Günnemann. Fast and  
632 uncertainty-aware directional message passing for non-equilibrium molecules. In *Machine Learn-  
633 ing for Molecules Workshop, NeurIPS*, 2020a.  
634
- 635 Johannes Gasteiger, Janek Groß, and Stephan Günnemann. Directional message passing for molecular  
636 graphs. *arXiv preprint arXiv:2003.03123*, 2020b.
- 637 Johannes Gasteiger, Florian Becker, and Stephan Günnemann. Gemnet: Universal directional  
638 graph neural networks for molecules. *Advances in Neural Information Processing Systems*, 34:  
639 6790–6802, 2021.  
640
- 641 Justin Gilmer, Samuel S Schoenholz, Patrick F Riley, Oriol Vinyals, and George E Dahl. Neural  
642 message passing for quantum chemistry. In *International conference on machine learning*, pp.  
643 1263–1272. PMLR, 2017.
- 644 Google Colaboratory. Google colaboratory: Free jupyter notebooks in the cloud. [https://colab.  
645 research.google.com/](https://colab.research.google.com/), 2023. Accessed: 2023-05-22.  
646
- 647 Branko Grünbaum. Graphs of polyhedra; polyhedra as graphs. *Discrete Mathematics*, 307(3-5):  
445–463, 2007.

- 648 Pedro Hermosilla, Marco Schäfer, Matěj Lang, Gloria Fackelmann, Pere Pau Vázquez, Barbora  
649 Kozlíková, Michael Krone, Tobias Ritschel, and Timo Ropinski. Intrinsic-extrinsic convolution  
650 and pooling for learning on 3d protein structures. *arXiv preprint arXiv:2007.06252*, 2020.  
651
- 652 Snir Hordan, Tal Amir, and Nadav Dym. Weisfeiler leman for euclidean equivariant machine learning.  
653 *arXiv preprint arXiv:2402.02484*, 2024.
- 654 Jie Hou, Badri Adhikari, and Jianlin Cheng. Deepsf: deep convolutional neural network for mapping  
655 protein sequences to folds. *Bioinformatics*, 34(8):1295–1303, 2018.  
656
- 657 Bowen Jing, Stephan Eismann, Patricia Suriana, Raphael John Lamarre Townshend, and Ron Dror.  
658 Learning from protein structure with geometric vector perceptrons. In *International Conference on*  
659 *Learning Representations*, 2020.
- 660 Peter Bjørn Jørgensen, Karsten Wedel Jacobsen, and Mikkel N Schmidt. Neural message passing with  
661 edge updates for predicting properties of molecules and materials. *arXiv preprint arXiv:1806.03146*,  
662 2018.  
663
- 664 Chaitanya K Joshi, Cristian Bodnar, Simon V Mathis, Taco Cohen, and Pietro Lio. On the expressive  
665 power of geometric graph neural networks. *arXiv preprint arXiv:2301.09308*, 2023.  
666
- 667 Thomas N. Kipf and Max Welling. Semi-supervised classification with graph convolutional networks.  
668 In *Proceedings of the 5th International Conference on Learning Representations*, 2017.
- 669 Gerard Laman. On graphs and rigidity of plane skeletal structures. *Journal of Engineering mathemat-*  
670 *ics*, 4(4):331–340, 1970.
- 671 Isaac E Leonard and James Edward Lewis. *Geometry of convex sets*. John Wiley & Sons, 2015.  
672
- 673 Michael Levitt and Cyrus Chothia. Structural patterns in globular proteins. *Nature*, 261(5561):  
674 552–558, 1976.
- 675 Jiahua Li. Directed weight neural networks for protein structure representation learning. *arXiv*  
676 *preprint arXiv:2201.13299*, 2022.  
677
- 678 Zian Li, Xiyuan Wang, Yinan Huang, and Muhan Zhang. Is distance matrix enough for geometric  
679 deep learning? *Advances in Neural Information Processing Systems*, 36, 2024.
- 680 Richard J Lipton and Robert Endre Tarjan. A separator theorem for planar graphs. *SIAM Journal on*  
681 *Applied Mathematics*, 36(2):177–189, 1979.  
682
- 683 Yi Liu, Limei Wang, Meng Liu, Yuchao Lin, Xuan Zhang, Bora Oztekin, and Shuiwang Ji. Spherical  
684 message passing for 3d molecular graphs. In *International Conference on Learning Representations*  
685 *(ICLR)*, 2022.
- 686 Zhihai Liu, Yan Li, Li Han, Jie Li, Jie Liu, Zhixiong Zhao, Wei Nie, Yuchen Liu, and Renxiao Wang.  
687 Pdb-wide collection of binding data: current status of the pddb database. *Bioinformatics*, 31(3):  
688 405–412, 2015.  
689
- 690 Amil Merchant, Simon Batzner, Samuel S Schoenholz, Muratahan Aykol, Gowoon Cheon, and  
691 Ekin Dogus Cubuk. Scaling deep learning for materials discovery. *Nature*, 624(7990):80–85,  
692 2023.
- 693 Boris Mityagin. The zero set of a real analytic function. *arXiv preprint arXiv:1512.07276*, 2015.  
694
- 695 Alexey G Murzin, Steven E Brenner, Tim Hubbard, and Cyrus Chothia. Scop: a structural classifica-  
696 tion of proteins database for the investigation of sequences and structures. *Journal of molecular*  
697 *biology*, 247(4):536–540, 1995.
- 698 Marina V Omelchenko, Michael Y Galperin, Yuri I Wolf, and Eugene V Koonin. Non-homologous  
699 isofunctional enzymes: a systematic analysis of alternative solutions in enzyme evolution. *Biology*  
700 *direct*, 5:1–20, 2010.  
701
- Joseph O’Rourke. *Computational geometry in C*. Cambridge University Press, 1998.

- 702 Priyadarshini Panda and Dipankar Pati. Spearman’s rank correlation: A comprehensive review  
703 and application. *International Journal of Engineering Science and Research Technology*, 4(11):  
704 143–148, 2015. doi: 10.5281/zenodo.1933629.
- 705  
706 Bryan Perozzi, Rami Al-Rfou, and Steven Skiena. Deepwalk: Online learning of social representa-  
707 tions. In *Proceedings of the 20th ACM SIGKDD international conference on Knowledge discovery*  
708 *and data mining*, pp. 701–710, 2014.
- 709 Victor Garcia Satorras, Emiel Hoogeboom, and Max Welling. E(n) equivariant graph neural networks.  
710 In *International conference on machine learning*, pp. 9323–9332. PMLR, 2021.
- 711  
712 Kristof Schütt, Pieter-Jan Kindermans, Huziel Enoc Saucedo Felix, Stefan Chmiela, Alexandre  
713 Tkatchenko, and Klaus-Robert Müller. Schnet: A continuous-filter convolutional neural network  
714 for modeling quantum interactions. *Advances in neural information processing systems*, 30, 2017.
- 715 Kristof T Schütt, Huziel E Saucedo, P-J Kindermans, Alexandre Tkatchenko, and K-R Müller.  
716 SchNet—a deep learning architecture for molecules and materials. *The Journal of Chemical Physics*,  
717 148(24), 2018.
- 718  
719 Amit Singer and Mihai Cucuringu. Uniqueness of low-rank matrix completion by rigidity theory.  
720 *SIAM Journal on Matrix Analysis and Applications*, 31(4):1621–1641, 2010.
- 721  
722 Vignesh Ram Somnath, Charlotte Bunne, and Andreas Krause. Multi-scale representation learning  
723 on proteins. *Advances in Neural Information Processing Systems*, 34:25244–25255, 2021.
- 724  
725 James J Stoker. Geometrical problems concerning polyhedra in the large. *Communications on pure*  
*and applied mathematics*, 21(2):119–168, 1968.
- 726  
727 Gürol M Süel, Steve W Lockless, Mark A Wall, and Rama Ranganathan. Evolutionarily conserved  
728 networks of residues mediate allosteric communication in proteins. *Nature structural biology*, 10  
729 (1):59–69, 2003.
- 730  
731 Yonatan Sverdlov and Nadav Dym. On the expressive power of sparse geometric mpnns. *arXiv*  
*preprint arXiv:2407.02025*, 2024.
- 732  
733 Raphael JL Townshend, Stephan Eismann, Andrew M Watkins, Ramya Rangan, Masha Karelina,  
734 Rhiju Das, and Ron O Dror. Geometric deep learning of rna structure. *Science*, 373(6558):  
735 1047–1051, 2021.
- 736  
737 John S. Uebersax. On the use of the pearson correlation coefficient for assessing agreement with  
738 ordinal data. *Journal of the Royal Statistical Society: Series C (Applied Statistics)*, 36(4):427–432,  
739 1987. doi: 10.2307/2347808.
- 740  
741 Oliver T Unke and Markus Meuwly. Physnet: A neural network for predicting energies, forces, dipole  
742 moments, and partial charges. *Journal of chemical theory and computation*, 15(6):3678–3693,  
743 2019.
- 744  
745 Pauli Virtanen, Ralf Gommers, Travis E. Oliphant, Matt Haberland, Tyler Reddy, David Cournapeau,  
746 Evgeni Burovski, Pearu Peterson, Warren Weckesser, Jonathan Bright, Stéfan J. van der Walt,  
747 Matthew Brett, Joshua Wilson, K. Jarrod Millman, Nikolay Mayorov, Andrew R. J. Nelson, Eric  
748 Jones, Robert Kern, Eric Larson, C J Carey, İlhan Polat, Yu Feng, Eric W. Moore, Jake VanderPlas,  
749 Denis Laxalde, Josef Perktold, Robert Cimrman, Ian Henriksen, E. A. Quintero, Charles R. Harris,  
750 Anne M. Archibald, Antônio H. Ribeiro, Fabian Pedregosa, Paul van Mulbregt, and SciPy 1.0  
751 Contributors. SciPy 1.0: Fundamental Algorithms for Scientific Computing in Python. *Nature*  
752 *Methods*, 17:261–272, 2020. doi: 10.1038/s41592-019-0686-2.
- 753  
754 Limei Wang, Haoran Liu, Yi Liu, Jerry Kurtin, and Shuiwang Ji. Learning hierarchical protein  
755 representations via complete 3d graph networks. *arXiv preprint arXiv:2207.12600*, 2022a.
- 756  
757 Limei Wang, Yi Liu, Yuchao Lin, Haoran Liu, and Shuiwang Ji. ComENet: Towards complete and  
758 efficient message passing for 3d molecular graphs. In Alice H. Oh, Alekh Agarwal, Danielle  
759 Belgrave, and Kyunghyun Cho (eds.), *Advances in Neural Information Processing Systems*, 2022b.  
760 URL <https://openreview.net/forum?id=mCzMqeWSFJ>.

756 Renxiao Wang, Xueliang Fang, Yipin Lu, and Shaomeng Wang. The pdbbind database: Collection of  
757 binding affinities for protein- ligand complexes with known three-dimensional structures. *Journal*  
758 *of medicinal chemistry*, 47(12):2977–2980, 2004.

759 Shih-Hsin Wang, Yung-Chang Hsu, Justin Baker, Andrea L. Bertozzi, Jack Xin, and Bao Wang.  
760 Rethinking the benefits of steerable features in 3d equivariant graph neural networks. In *The Twelfth*  
761 *International Conference on Learning Representations*, 2024. URL [https://openreview.](https://openreview.net/forum?id=mGHJAyR8w0)  
762 [net/forum?id=mGHJAyR8w0](https://openreview.net/forum?id=mGHJAyR8w0).

763 Emo Welzl, H. Alt, Kurt Mehlhorn, and Hubert Wagener. Congruence, similarity, and symmetries  
764 of geometric objects. *Discrete & computational geometry*, 3(3):237–256, 1988. URL [http:](http://eudml.org/doc/131048)  
765 [//eudml.org/doc/131048](http://eudml.org/doc/131048).

766 Zuobai Zhang, Minghao Xu, Arian Jamasb, Vijil Chenthamarakshan, Aurelie Lozano, Payel Das,  
767 and Jian Tang. Protein representation learning by geometric structure pretraining. *arXiv preprint*  
768 *arXiv:2203.06125*, 2022.

769 Jingxuan Zhu, Juexin Wang, Weiwei Han, and Dong Xu. Neural relational inference to learn  
770 long-range allosteric interactions in proteins from molecular dynamics simulations. *Nature*  
771 *communications*, 13(1):1661, 2022.

772  
773  
774  
775  
776  
777  
778  
779  
780  
781  
782  
783  
784  
785  
786  
787  
788  
789  
790  
791  
792  
793  
794  
795  
796  
797  
798  
799  
800  
801  
802  
803  
804  
805  
806  
807  
808  
809

## A ADDITIONAL RELATED WORKS.

**Invariant graph neural networks and completeness of geometric attributes.** Invariant graph neural networks (GNNs) have emerged as powerful tools for analyzing geometric graphs by leveraging invariant geometric features (attributes) that remain unchanged under transformations like rotation and translation. The effectiveness of invariant GNNs hinges on the development of such features that not only remain invariant but also truly capture the essential geometric information carried by the graph. Several studies have explored methods for learning different meaningful invariant geometric features that effectively capture the underlying geometric structure of the data. SchNet (Schütt et al., 2018) utilizes pairwise distances between nodes as basic invariant geometric attributes. SphereNet (Liu et al., 2022) employs a local spherical coordinate system around each node to generate invariant distance and angular features. GemNet (Gasteiger et al., 2021) and ComENet (Wang et al., 2022b) incorporate torsion angles computed on node quadruplets, which is particularly useful for predicting the properties of molecular conformers. Similar to the way torsion angles capture the angles between local structures, LEFTNet (Du et al., 2024) leverages local frames centered on each node, allowing them to scalarize all spatial information into a set of invariant features and then combine them with frame transition information to capture global features.

Notably, Wang et al. (2022b) introduced the notion of completeness of geometric attributes on the graph, which is closely related to rigidity. Geometric attributes on the graph are considered complete if they can uniquely determine the spatial arrangement of the nodes within the graph. In fact, Wang et al. (2022b) demonstrated that their proposed framework ComENet is complete. However, as noted in (Wang et al., 2024), most existing methods, including all the models mentioned above, rely on fixed-size neighborhoods, which may be insufficient to capture all relevant global geometric features. While our graph rigidity proof hinges on the assumption of generic point clouds, it’s crucial to recognize that the graph structure, formed through a global assessment of geometric arrangement, cannot be inferred solely from local information.

**Power graphs.** The  $k^{\text{th}}$ -power graph of a given graph connects any two nodes if there exists a path between them in the original graph with length  $\leq k$ . Sverdlov & Dym (2024) propose 4<sup>th</sup>-power graphs as a potential solution to achieve rigidity in 3D geometric graphs. While power graphs may offer a potential approach to achieve rigidity in generic point clouds, they can lead to overly dense graphs, which can be inefficient for large-scale structures. Additionally, power graphs require the original graph to be connected for the resulting power graph to remain connected. Furthermore, they may fail to help GNNs distinguish between two ambiguous, non-generic point clouds. These limitations are demonstrated in Tables 6 and 7.

**High-order graphs.** Several studies have explored incorporating higher-order structures into graphs to capture more detailed geometric information. Notable examples include simplicial complexes (Eijkelboom et al., 2023) and combinatorial complexes (Battiloro et al., 2024). While these approaches show promise for encoding and learning geometric properties, they often suffer from high computational complexity during their construction, making them less efficient than our approach, especially when dealing with large proteins, along with other potential limitations. Specifically, simplicial complexes, constructed in (Eijkelboom et al., 2023), rely on radius-based connectivity, which may not guarantee connectivity (and hence may not guarantee rigidity) in all cases, as shown in Fig. 1. However, it would be interesting to explore how our graph construction method could be used as a foundation for generating simplicial complexes and how these resulting complexes might perform in capturing geometric and structural properties. Combinatorial complexes provide a more general framework for higher-order structures, encompassing simplicial complexes as a subset. Of particular interest is the concept of molecular combinatorial complexes introduced in (Battiloro et al., 2024). These complexes incorporate atoms, bonds, rings, and functional groups as cells of complexes. Developing invariant features to ensure the rigidity of these complexes presents an exciting avenue for future research. To the best of our knowledge, however, no prior work has explored this direction. We believe it would be worthwhile to investigate whether sparse, connected, and rigid simplicial or combinatorial complexes can be effectively constructed and applied in higher-order models.

**Graph construction for symmetric detections** The graph construction method we propose shares similarities with the one introduced in (Welzl et al., 1988) for symmetric detection. However, our approach defines the graph on the original point clouds, rather than solely on the projected point clouds as in the referenced work. Furthermore, our design of graph attributes differs significantly: while Welzl et al. (1988) use interior angles of facets, we employ dihedral angles between facets as the key attribute in our graph construction.



## B ADDITIONAL DISCUSSIONS

**Non-generic point clouds.** Several existing works have explored the expressivity of GNNs on non-generic point clouds. For instance,  $k$ -DisGNNs (Li et al., 2024) aim to address the limitations of GNNs in fully leveraging the distance graph (i.e., a complete graph with distance as edge attributes) by designing higher-order GNN models that can better distinguish non-generic point clouds. Similarly, Hordan et al. (2024) propose WeLNet, which utilizes the distance graph and provides a theoretical guarantee that it can distinguish between all non-isometric 3D point clouds.

In this section, we apply our method to non-generic point clouds, particularly focusing on symmetric point clouds to assess if it improves traditional GNNs’ ability to distinguish them. Prior work, such as (Li et al., 2024), has shown that even when distances are incorporated into a complete graph – where every pair of nodes is connected – GNNs can still struggle with special cases, such as collections of nodes from the vertices of convex regular polyhedrons.

To investigate whether incorporating our SCHull graph addresses these challenges, we test it using counterexamples of 6-point and 14-point configurations from (Li et al., 2024); see Fig. 6 for a visualization. Specifically, we adapt the EGNN architecture from (Satorras et al., 2021) by removing equivariant updates and replacing edge attributes with invariant features such as distances and dihedral angles. Experiments were conducted on a dataset consisting of augmented counterexample pairs, each subjected to 20 random rotations, over 100 epochs, with results averaged over 10 independent runs. We report the mean accuracy and standard deviation to ensure robustness. The empirical results in Tables 6 and 7 demonstrate that the edge attribute design of the SCHull graph (equation (5)) enables even shallow GNNs to distinguish between two non-isomorphic geometric graphs successfully.

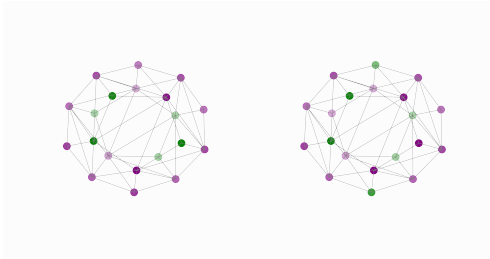


Figure 6: Visualization of pairs of 6-point (green) and 14-point (purple) configurations from (Li et al., 2024), where the edges represent the dodecahedron.

To provide further validation and comparisons, we have also tested the efficacy of using only edge distances within the SCHull graph and evaluated alternative graph construction methods, including radial cutoff graphs with varying thresholds, power graphs (Sverdlov & Dym, 2024), and complete graphs (Li et al., 2024; Hordan et al., 2024). The graph properties and performance for all methods are summarized in Tables 6 and 7, with tuple notations representing distinct graph properties on paired point clouds. Additionally, visualizations of the graphs for the 14-point configurations are provided in Table 8, offering a clearer geometric perspective on the differences between the approaches.

	1 Layer	2 Layers	# Edges / # Nodes	# Components
Radius Graph ( $r = 1.8$ ) w/ Distance	50.0 $\pm$ 0.0	50.0 $\pm$ 0.0	0.33	4
Radius Graph ( $r = 2.5$ ) w/ Distance	50.0 $\pm$ 0.0	50.0 $\pm$ 0.0	1	(2, 1)
Radius Graph ( $r = 3.0$ ) w/ Distance	50.0 $\pm$ 0.0	50.0 $\pm$ 0.0	1.67	1
4 <sup>th</sup> -power Radius Graph ( $r = 1.8$ ) w/ Distance	50.0 $\pm$ 0.0	50.0 $\pm$ 0.0	0.33	4
4 <sup>th</sup> -power Radius Graph ( $r = 2.5$ ) w/ Distance	<b>100.0 <math>\pm</math> 0.0</b>	<b>100.0 <math>\pm</math> 0.0</b>	(1, 2.5)	(2, 1)
4 <sup>th</sup> -power Radius Graph ( $r = 3.0$ ) w/ Distance	50.0 $\pm$ 0.0	50.0 $\pm$ 0.0	2.5	1
Complete Graph w/ Distance	50.0 $\pm$ 0.0	50.0 $\pm$ 0.0	2.5	1
SCHull w/ Distance	50.0 $\pm$ 0.0	50.0 $\pm$ 0.0	2.0	1
SCHull w/ Distance and Dihedral Angles	<b>100.0 <math>\pm</math> 0.0</b>	<b>100.0 <math>\pm</math> 0.0</b>	2.0	1

Table 6: Comparison of graph properties and GNN performance (Unit:%) on 6-point symmetric point clouds using different graph construction methods. Tuple notations represent distinct graph properties on paired point clouds.

The results showcase the limitations of alternative methods: radius graphs face issues of disconnectivity at small radii and edge redundancy at larger radii, neither of which ensures consistent performance; power graphs exhibit inconsistent performance that depends heavily on careful parameter tuning, and they fail to address issues of sparsity or connectivity effectively; complete graphs – while providing exhaustive connectivity – are computationally expensive and do not improve accuracy. In contrast, the SCHull graph achieves a balance of sparsity and rigidity, offering a compact yet expressive

	1 Layer	2 Layers	# Edges / # Nodes	# Components
Radius Graph ( $r = 1.8$ ) w/ $d_{ij}$	$50.0 \pm 0.0$	$50.0 \pm 0.0$	1.0	(1, 2)
Radius Graph ( $r = 2.5$ ) w/ $d_{ij}$	$50.0 \pm 0.0$	$51.0 \pm 3.0$	3.0	1
Radius Graph ( $r = 3.0$ ) w/ $d_{ij}$	$60.5 \pm 11.1$	$57.2 \pm 9.1$	5.0	1
4 <sup>th</sup> -power Radius Graph ( $r = 1.8$ ) w/ $d_{ij}$	<b><math>100.0 \pm 0.0</math></b>	<b><math>100.0 \pm 0.0</math></b>	(5, 3)	(1, 2)
4 <sup>th</sup> -power Radius Graph ( $r = 2.5$ ) w/ $d_{ij}$	$50.0 \pm 0.0$	$50.0 \pm 0.0$	6.5	1
4 <sup>th</sup> -power Radius Graph ( $r = 3.0$ ) w/ $d_{ij}$	$50.0 \pm 0.0$	$50.0 \pm 0.0$	6.5	1
Complete Graph w/ $d_{ij}$	$59.0 \pm 6.6.0$	$50.0 \pm 0.0$	6.5	1
SCHull w/ $d_{ij}$	<b><math>100.0 \pm 0.0</math></b>	<b><math>100.0 \pm 0.0</math></b>	2.57	1
SCHull w/ $d_{ij}$ and $\tau_{ij}$	<b><math>100.0 \pm 0.0</math></b>	<b><math>100.0 \pm 0.0</math></b>	2.57	1

Table 7: Comparison of graph properties and GNN performance (Unit:%) on 14-point symmetric point clouds using different graph construction methods. Tuple notations represent distinct graph properties on paired point clouds.

representation that enhances GNN performance. Its efficiency and scalability make it particularly appealing for large datasets, enabling effective learning with minimal computational overhead.

These findings emphasize the SCHull graph’s robustness and efficiency in distinguishing symmetric point clouds, confirming its design as both expressive and computationally efficient. However, a formal theoretical analysis of this approach for non-generic point clouds is left as a direction for future work.

**Geometric Interpretation.** We present an intuitive explanation of the SCHull graph construction to clarify its connection to the convex hull and its advantages in representing point clouds.

The convex hull captures only the outermost boundary of a point cloud, omitting information about interior points. This is evident in Fig. 7, where the convex hull of  $\{\mathbf{x}_i\}_{i=1}^6$  (left) aligns with the SCHull graph for those points. However, for  $\{\mathbf{x}_i\}_{i=1}^8$  (right), the convex hull remains the same as for  $\{\mathbf{x}_i\}_{i=1}^6$ , failing to account for interior points  $\mathbf{x}_7, \mathbf{x}_8$ . In contrast, SCHull connects interior points, preserving the structural relationships necessary to recover both the convex hull and the full geometry of the point cloud.

SCHull’s design addresses this limitation by leveraging spherical projection. Points are mapped onto the unit sphere, where the graph structure is computed. This ensures that interior points contribute to the graph’s structure. Conceptually, this transformation is akin to converting 3D Cartesian coordinates  $(x, y, z)$  into spherical coordinates  $(r, \theta, \phi)$ , where the radial distance  $r$  is excluded in the graph construction. The SCHull graph, therefore, relies only on the angular coordinates  $(\theta, \phi)$ , capturing the intrinsic geometry of the point cloud. One can see this rationale through the polar grid in Fig. 7. Importantly, the radial coordinate  $r$  is retained as a node feature. This allows for the reconstruction of the original 3D coordinates  $(r, \theta, \phi)$  and allows SCHull to represent global geometric properties effectively. For example, as shown in Fig. 7, edge lengths like  $\|\mathbf{x}_1 - \mathbf{x}_7\|$  and  $\|\mathbf{x}_1 - \mathbf{x}_6\|$  can be used together with node features  $\|\mathbf{x}_1\|, \|\mathbf{x}_6\|, \|\mathbf{x}_7\|$  to compute information on the convex hull, such as  $\|\mathbf{x}_1 - \mathbf{x}_6\|$ .

In summary, SCHull preserves the global geometry of the convex hull while enriching it with the structural representation of interior points. This makes SCHull an effective tool for capturing the full spatial structure of point clouds and their intrinsic relationships. We note that Fleming & Fleming (2018) uses the convex hull to estimate hydrodynamic volume, and we believe that the SCHull graph could not only improve the prediction of this property but also offer additional insights.

**Discontinuous intrinsic properties of graph construction.** The discrete nature of graph data inherently prevents the possibility of truly continuous graph construction, a limitation shared by all graph construction methods, including the one proposed in this work. While this was not the primary focus of our discussion, it raises an intriguing question: how does the choice of graph construction, especially those with attribute designs, affect the smoothness properties of end-to-end neural network models? Specifically, if the input data is perturbed by noise or errors, can we theoretically analyze how different graph construction methods influence the resulting impact on the neural network’s output? For instance, does the output exhibit stability under input perturbations such that the end-to-end models are still continuous?

972  
973  
974  
975  
976  
977  
978  
979  
980  
981  
982  
983  
984  
985  
986  
987  
988  
989  
990  
991  
992  
993  
994  
995  
996  
997  
998  
999  
1000  
1001  
1002  
1003  
1004  
1005  
1006  
1007  
1008  
1009  
1010  
1011  
1012  
1013  
1014  
1015  
1016  
1017  
1018  
1019  
1020  
1021  
1022  
1023  
1024  
1025

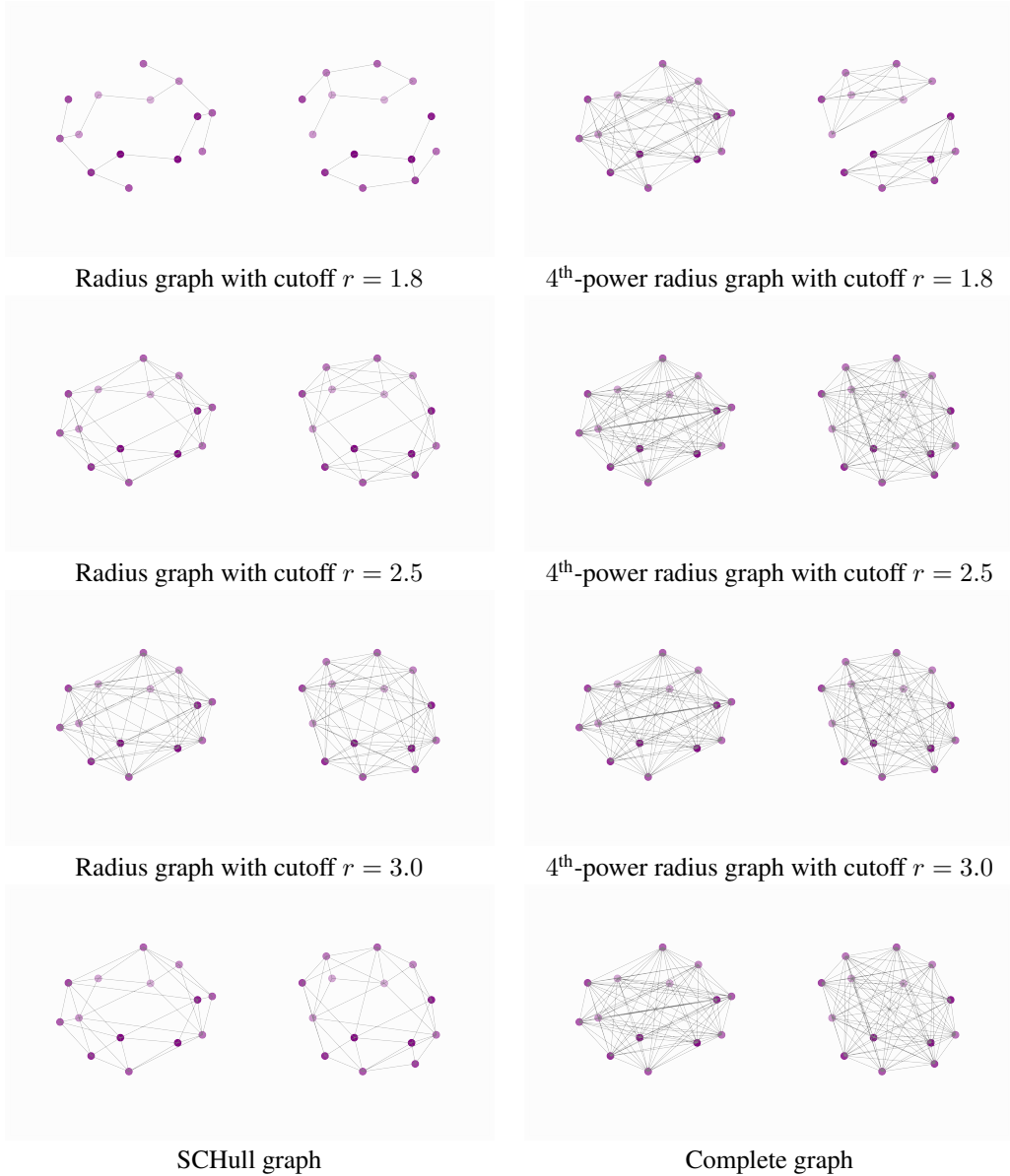


Table 8: We visualize the graphs of 14-points point clouds used in the experiments whose graph properties and performance with GNNs are presented in Table 7.

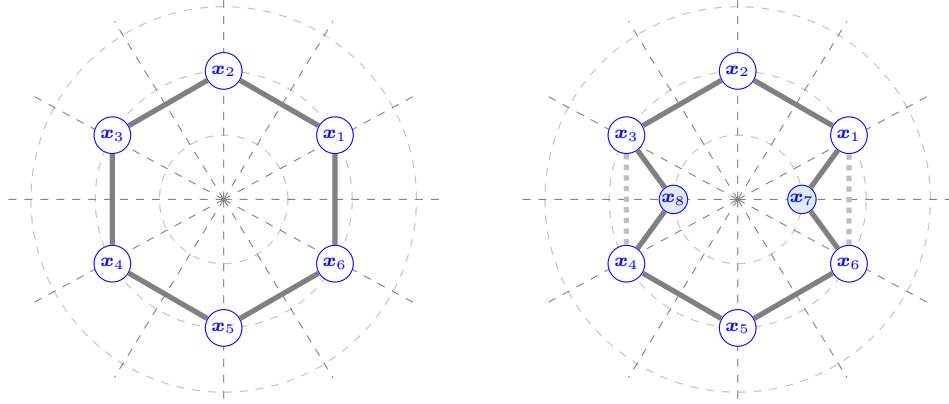


Figure 7: This figure highlights the close relationship between the convex hull of point clouds and SCHull graphs. While the convex hull captures only the outer boundary, potentially discarding information about interior points, the SCHull graph retains this information by connecting interior points. The edges of the SCHull graph are represented by solid gray lines, while the dashed gray lines indicate convex hull edges that differ from those of the SCHull graph. This distinction emphasizes SCHull’s ability to preserve and enrich geometric relationships beyond the convex hull.

## C MISSING PROOFS AND ADDITIONAL DETAILS

**Proposition 3.1.** *Let  $\mathcal{Z} = \{z_j\}$  be a set of points on a sphere where  $|\mathcal{Z}| \geq 3$  (the number of points is at least 3), and let  $\text{Conv}(\mathcal{Z})$  denote the convex hull of  $\mathcal{Z}$  with its associated graph structure consisting of nodes, edges, and faces defined by its boundary. Then, we have*

1. *Connectivity: Any two points in  $\mathcal{Z}$  are connected by a sequence of edges in  $\text{Conv}(\mathcal{Z})$ .*
2. *Sparsity: The number of edges in  $\text{Conv}(\mathcal{Z})$  is no greater than  $3|\mathcal{Z}| - 6$ .*

Moreover,  $\text{Conv}(\mathcal{Z})$  is a strictly convex geometric polyhedral graph if  $z_j$ s are not coplanar.

*Proof of Proposition 3.1.* Since the point cloud  $\mathcal{Z}$  lies on a sphere, each point in  $\mathcal{Z}$  is an extreme point (Leonard & Lewis, 2015) of  $\text{Conv}(\mathcal{Z})$ . Consequently, each point appears as a node in the graph structure of the convex hull. If the points in  $\mathcal{Z}$  are not coplanar, then  $\text{Conv}(\mathcal{Z})$  is a convex polyhedron, and, hence by definition,  $\text{Conv}(\mathcal{Z})$  is a strictly convex polyhedral graph. Since each convex polyhedron can be represented as a 3-connected planar graph by Steinitz’s theorem,  $\text{Conv}(\mathcal{Z})$  is connected, and the number of its edges is bounded above by  $3|\mathcal{Z}| - 6$  (Lipton & Tarjan, 1979; O’Rourke, 1998). If the points in  $\mathcal{Z}$  are coplanar, then  $\text{Conv}(\mathcal{Z})$  itself is a connected planar graph. Therefore, the same bound of  $3|\mathcal{Z}| - 6$  on the number of edges holds.  $\square$

**Lemma 3.4.** *Any generic point cloud satisfies the generic assumption equation (3).*

*Proof of Lemma 3.4.* If  $x_i = \bar{x}$  for some  $i \in \mathcal{V}$ , it directly defines a linear algebraic dependence on the coordinates, leading to a contradiction. Similarly, suppose  $p_{\bar{x}}(x_i) = p_{\bar{x}}(x_j)$  for some  $i, j \in \mathcal{V}$ . Then we have  $\frac{(x_i - \bar{x})}{\|(x_i - \bar{x})\|} = \frac{(x_j - \bar{x})}{\|(x_j - \bar{x})\|}$ , implying that  $(x_i - \bar{x}) \cdot (x_j - \bar{x}) = \|x_i - \bar{x}\| \|x_j - \bar{x}\|$ . Taking the square of both sides, we obtain an algebraic dependence on the coordinates, which leads to a contradiction.  $\square$

**Lemma 3.5.** *Let  $(\mathcal{V}, X)$  be a generic point cloud. Then  $\text{Conv}(\{p_{\bar{x}}(x_i) \mid i \in \mathcal{V}\})$  – the convex hull on the sphere we constructed in Section 3.1 – is a strictly convex geometric polyhedral graph.*

*Proof of Lemma 3.5.* Due to Proposition 3.1, it suffices to show that  $\{p_{\bar{x}}(x_i) \mid i \in \mathcal{V}\}$  are not coplanar. This is true unless the original point cloud lies on a plane, which contradicts the genericity assumption.  $\square$

**Theorem 3.6.** *Let  $F$  be a maximally expressive GNN with depth  $T = 1$ . Then  $F$  can distinguish between the attributed SCHull graphs defined in equation (5) of any two non-isomorphic generic point clouds.*

*Proof of Theorem 3.6.* The proof is inspired by the work Sverdllov & Dym (2024). Consider two SCHull graphs,  $\mathcal{G}$  and  $\mathcal{G}'$ , generated from point clouds  $(\mathcal{V}, \mathbf{X})$  and  $(\mathcal{V}', \mathbf{X}')$ , respectively. If the maximally expressive GNN  $F$  assigns the same global feature to  $\mathcal{G}$  and  $\mathcal{G}'$  after one iteration, then the multisets of node features  $\{s_i\}$  and  $\{s'_i\}$  are identical. This implies  $|\mathcal{V}| = |\mathcal{V}'|$ . By relabeling, if necessary, we can assume that  $s_i = s'_i$  for all  $i \in \mathcal{V}$ . This further implies that for each node  $i \in \mathcal{V}$ , the node features  $\mathbf{f}_i = \mathbf{f}'_i$  and the multisets of edge features  $\{e_{ij} \mid j \in \mathcal{N}_i\} = \{e'_{ij} \mid j \in \mathcal{N}'_i\}$  are also the same. That is,  $\|\mathbf{x}_i - \bar{\mathbf{x}}\| = \|\mathbf{x}'_i - \bar{\mathbf{x}}'\|$  and  $\{(\|\mathbf{x}_i - \mathbf{x}_j\|, \tau_{ij}) \mid j \in \mathcal{N}_i\} = \{(\|\mathbf{x}'_i - \mathbf{x}'_j\|, \tau'_{ij}) \mid j \in \mathcal{N}'_i\}$ . Notice that the number of edges  $|\mathcal{E}|$  is equal to  $\frac{1}{2} \sum_i d_i$ , where  $d_i$  denotes the degree of the node  $i$ . Since the degrees of corresponding nodes on graphs  $\mathcal{G}, \mathcal{G}'$  are equal, both graphs have the same sum of node degrees and hence the same number of edges, i.e.,  $|\mathcal{E}| = |\mathcal{E}'|$ . Due to the generic nature of point clouds, for any edge  $(i, j) \in \mathcal{E}$ , the distance  $\|\mathbf{x}'_i - \mathbf{x}'_j\|$  will appear exactly once in the multisets corresponding to nodes  $i$  and  $j$  on both graphs. This means that  $(i, j)$  is also an edge in  $\mathcal{E}'$  and hence the underlying graph  $(\mathcal{V}, \mathcal{E})$  and  $(\mathcal{V}', \mathcal{E}')$  are isomorphic. It also follows that the edge attributes of corresponding edges are the same, i.e.,  $\|\mathbf{x}_i - \mathbf{x}_j\| = \|\mathbf{x}'_i - \mathbf{x}'_j\|$  and  $\tau_{ij} = \tau'_{ij}$ . Next, we observe that the triple  $(\|\mathbf{x}_i - \mathbf{x}_j\|, \|\mathbf{x}_i - \bar{\mathbf{x}}\|, \|\mathbf{x}_j - \bar{\mathbf{x}}\|)$  uniquely determines the distance between projected points  $p_{\bar{\mathbf{x}}}(\mathbf{x}_i), p_{\bar{\mathbf{x}}}(\mathbf{x}_j)$  on the unit sphere as we show in Lemma C.1 below. Therefore, the equality between triples  $(\|\mathbf{x}_i - \mathbf{x}_j\|, \|\mathbf{x}_i - \bar{\mathbf{x}}\|, \|\mathbf{x}_j - \bar{\mathbf{x}}\|) = (\|\mathbf{x}'_i - \mathbf{x}'_j\|, \|\mathbf{x}'_i - \bar{\mathbf{x}}'\|, \|\mathbf{x}'_j - \bar{\mathbf{x}}'\|)$  implies  $\|p_{\bar{\mathbf{x}}}(\mathbf{x}_i) - p_{\bar{\mathbf{x}}}(\mathbf{x}_j)\| = \|p_{\bar{\mathbf{x}}'}(\mathbf{x}'_i) - p_{\bar{\mathbf{x}}'}(\mathbf{x}'_j)\|$ . Combined with the identity  $\tau_{ij} = \tau'_{ij}$  and the fact that  $(\mathcal{V}, \mathcal{E})$  and  $(\mathcal{V}', \mathcal{E}')$  are isomorphic, we can conclude that  $(\mathcal{V}, \mathcal{E}, p_{\bar{\mathbf{x}}}(\mathbf{X}))$  and  $(\mathcal{V}', \mathcal{E}', p_{\bar{\mathbf{x}}'}(\mathbf{X}'))$  are geometrically isomorphic using Lemma 3.5 and Theorem 2.1. Finally, because we can recover the original coordinates  $\mathbf{X}$  from the projected points  $p_{\bar{\mathbf{x}}}(\mathbf{X})$  by  $\|\mathbf{x}_i - \bar{\mathbf{x}}\| \cdot p_{\bar{\mathbf{x}}}(\mathbf{x}_i) = \mathbf{x}_i$ ,  $(\mathcal{V}, \mathcal{E}, \mathbf{X}, \mathbf{F})$  and  $(\mathcal{V}', \mathcal{E}', \mathbf{X}', \mathbf{F}')$  are also geometrically isomorphic.  $\square$

**Lemma C.1.** *The triple  $(\|\mathbf{x}_i - \mathbf{x}_j\|, \|\mathbf{x}_i - \bar{\mathbf{x}}\|, \|\mathbf{x}_j - \bar{\mathbf{x}}\|)$  uniquely determines the distance between projected points  $p_{\bar{\mathbf{x}}}(\mathbf{x}_i), p_{\bar{\mathbf{x}}}(\mathbf{x}_j)$  on the unit sphere.*

*Proof of Lemma C.1.* We denote the projection  $p_{\bar{\mathbf{x}}}$  by  $p$  for simplicity. Notice that the angle formed by the vertices  $\mathbf{x}_i, \bar{\mathbf{x}}, \mathbf{x}_j$  is the same as the angle formed by the vertices  $p(\mathbf{x}_i), \bar{\mathbf{x}}, p(\mathbf{x}_j)$ , since projection  $p$  preserves the angle subtended by these points. Denote this angle by  $\alpha$ . Following the Law of Cosines, we have:

$$\cos(\alpha) = \frac{\|\mathbf{x}_i - \bar{\mathbf{x}}\|^2 + \|\mathbf{x}_j - \bar{\mathbf{x}}\|^2 - \|\mathbf{x}_i - \mathbf{x}_j\|^2}{2\|\mathbf{x}_i - \bar{\mathbf{x}}\| \cdot \|\mathbf{x}_j - \bar{\mathbf{x}}\|} \quad (6)$$

and

$$\|p(\mathbf{x}_i) - p(\mathbf{x}_j)\|^2 = \|p(\mathbf{x}_i) - \bar{\mathbf{x}}\|^2 + \|p(\mathbf{x}_j) - \bar{\mathbf{x}}\|^2 - 2\|p(\mathbf{x}_i) - \bar{\mathbf{x}}\|\|p(\mathbf{x}_j) - \bar{\mathbf{x}}\| \cos(\alpha) \\ = 2 - 2 \cos(\alpha), \quad (7)$$

where we have used the fact that  $\|p(\mathbf{x}_i) - \bar{\mathbf{x}}\| = 1$  and  $\|p(\mathbf{x}_j) - \bar{\mathbf{x}}\| = 1$  as both points lie on the unit sphere. From equation (6), we can compute  $\cos(\alpha)$  using the given triple  $(\|\mathbf{x}_i - \mathbf{x}_j\|, \|\mathbf{x}_i - \bar{\mathbf{x}}\|, \|\mathbf{x}_j - \bar{\mathbf{x}}\|)$ . Substituting this value of  $\cos(\alpha)$  into equation (7), we can then solve for  $\|p(\mathbf{x}_i) - p(\mathbf{x}_j)\|$ , which gives the distance between the projected points.  $\square$

## D MAINTAINING THE CONNECTIVITY OF SCHULL

In the SCHull graph construction presented in the main text, we assume the following condition holds:

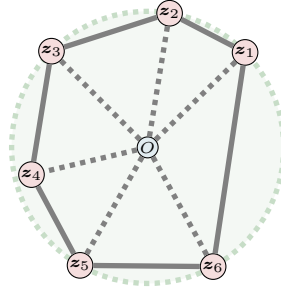
$$\mathbf{x}_i \neq \bar{\mathbf{x}} \text{ and } p_{\bar{\mathbf{x}}}(\mathbf{x}_i) \neq p_{\bar{\mathbf{x}}}(\mathbf{x}_j) \text{ for any } i \neq j \in \mathcal{V}. \quad (8)$$

Here, we outline a strategy to maintain the connectivity and sparsity of our graph when the generic condition equation (3) does not hold.

1134 **When  $x_i = \bar{x}$  for some node  $i$ :** To preserve graph connectivity, we employ a strategy similar to  
 1135  $k$ -nearest neighbors. We connect  $x_i$  to its nearest neighbor(s) in the point cloud. Unless there is  
 1136 a significant number of points exactly at the center of the point cloud, this modification will not  
 1137 substantially compromise sparsity.

1138 **When  $p_{\bar{x}}(x_i) \neq p_{\bar{x}}(x_j)$  for some nodes  $i, j$ :** In these cases, we compare the norms  $\|x_i\|$  and  $\|x_j\|$ .  
 1139 If  $\|x_i\| > \|x_j\|$ , we treat  $x_i$  as the representative of the point  $p_{\bar{x}}(x_i)$  on the unit sphere and then  
 1140 connect edges to  $x_i$  following the original SCHull graph construction. Subsequently, we connect  $x_j$   
 1141 to  $x_i$ . This approach ensures that sparsity is preserved.

## 1143 E SCHULL GRAPHS OF 2D POINT CLOUDS.



1144  
1145  
1146  
1147  
1148  
1149  
1150  
1151  
1152  
1153  
1154  
1155 **Figure 8:** A visualization illustrating how the edge lengths of a polygon on the unit circle uniquely determine  
 1156 the spatial arrangement of its vertices.

1157  
1158 When a point cloud lies on the plane, its associated SCHull graph corresponds to a polygon, with  
 1159 each vertex positioned on the unit circle, as illustrated in Fig. 8. In this case, the dihedral angles, as  
 1160 defined in equation (5), become zero since there is only a single facet.

1161 Nevertheless, the SCHull graph with edge attributes  $\|x_i - x_j\|$  and node attributes  $\|x_i - \bar{x}\|$  provides  
 1162 sufficient information for a maximally expressive GNN to distinguish non-isomorphic generic point  
 1163 clouds on the plane. Here the genericity of point clouds (Definition 3.3) is characterized by 2D  
 1164 coordinates on the plane. The formal result is stated in the following theorem:

1165 **Theorem E.1.** *Let  $F$  be a maximally expressive GNN with depth  $T = 1$ . Then,  $F$  can distinguish*  
 1166 *between the attributed SCHull graphs defined in equation (5) of any two non-isomorphic generic*  
 1167 *point clouds on the plane.*

1168  
1169 The proof of this theorem follows a similar approach to Theorem 3.6, relying on an analogous result  
 1170 to Theorem 2.1 for polygons on the unit circle. Specifically, we need to show that the edge lengths of  
 1171 a polygon uniquely determine its structure on the unit circle, up to isometry:

1172 **Lemma E.2.** *The coordinates of the vertices of an  $n$ -polygon inscribed in a circle are uniquely*  
 1173 *determined by the sequence of its edge lengths, up to isometry.*

1174  
1175 *Proof of Lemma E.2.* Let the coordinates of the vertices on the circle be denoted as  $z_1, z_2, \dots, z_n$ ,  
 1176 ordered counterclockwise. We aim to show that the edge lengths  $\|z_{i+1} - z_i\|$  for  $1 \leq i \leq n-1$  and  
 1177  $\|z_1 - z_n\|$  are sufficient to uniquely determine the vertices  $z_1, z_2, \dots, z_n$ , up to isometry. Each edge  
 1178 length  $\|z_{i+1} - z_i\|$  determines the triangle formed by  $z_i, z_{i+1}$ , and the circle’s center  $O$  using the  
 1179 side-side-side (SSS) triangle congruence criterion. Similarly, the edge length  $\|z_1 - z_n\|$  determines  
 1180 the triangle formed by  $z_n, z_1$ , and  $O$ . By sequentially composing these triangles in order, the shape of  
 1181 the entire polygon is fully determined by Cauchy’s Arm Lemma (Chern, 1967) up to isometry. A  
 1182 visualization is demonstrated in Fig. 8.  $\square$

1183  
1184 *Proof of Theorem E.1.* Following the same steps as in the proof of Theorem 3.6, we first establish  
 1185 that the underlying graphs  $(\mathcal{V}, \mathcal{E})$  and  $(\mathcal{V}', \mathcal{E}')$ . Additionally, the distances between corresponding  
 1186 nodes satisfy  $\|p_{\bar{x}}(x_i) - p_{\bar{x}}(x_j)\| = \|p_{\bar{x}'}(x'_i) - p_{\bar{x}'}(x'_j)\|$ . From the graph structure of the polygons,  
 1187 it follows that the sequence of edge lengths is identical for the two graphs. By Lemma E.2, this  
 implies that the projected point clouds on the circle are identical up to isometry. Using the node



features  $\{\|\mathbf{x}_i - \bar{\mathbf{x}}\|\}$  and  $\{\|\mathbf{x}'_i - \bar{\mathbf{x}}'\|\}$ , we conclude that the underlying point clouds are identical up to isometry.  $\square$

## F RIGIDITY OF ATTRIBUTED SCHULL GRAPHS WITHOUT NODE ATTRIBUTES

In Section 3.3, we demonstrated that the attributed design defined in equation (5) is sufficient for maximally expressive GNNs to distinguish non-isomorphic generic point clouds in Theorem 3.6. Here, we investigate when the node attributes  $f_i, \|\mathbf{x}_i - \bar{\mathbf{x}}\|$ , representing the original distance of each point to the center of the point cloud, can be omitted. We will show that edge lengths and dihedral angles are sufficient to guarantee rigidity of SCHull graphs of generic point clouds under the following additional generic assumption:

$$\text{Any four projected points } \{p_{\bar{\mathbf{x}}}(\mathbf{x}_i)\} \text{ are not coplanar.} \quad (9)$$

Point clouds that do not satisfy this condition are included in a finite union of zero sets of analytic functions, which has Lebesgue measure zero (Mityagin, 2015).

Specifically, we aim to prove the following theorem:

**Theorem F.1.** *Let  $F$  be a maximally expressive GNN with depth  $T = 1$ . Then  $F$  can distinguish between the SCHull graphs using only edge-attributes defined in equation (5) of any two non-isomorphic generic point clouds satisfying equation (9).*

Note that the proof of Theorem 3.6 relies on the rigidity of strictly-convex geometric polyhedral graphs stated in Theorem 2.1. Similarly, our proof of Theorem F.1 relies on the following rigidity theorem for geometric polyhedral graphs from (Cho & Kim, 2023):

**Theorem F.2.** *If a geometric, possibly nonconvex and self-intersecting, polyhedral graph satisfies that (i) every face is convex, (ii) there are no coplanar adjacent faces and no set of seven vertices lies on the same plane, and (iii) any triple of vertices is not collinear, then its geometric arrangement is uniquely determined up to rigid motions by its dihedral angles and edge lengths.*

To prove Theorem F.1, it suffices to show that generic point clouds satisfying equation (9) fulfill the required conditions in Theorem F.2.

First, the genericity of point clouds ensures the conditions (ii) and (iii), as they can be expressed as polynomials of points' coordinates with rational coefficients. To demonstrate that all faces on the SCHull graph are convex, we observe that since any four projected points  $\{p_{\bar{\mathbf{x}}}(\mathbf{x}_i)\}$  are not coplanar, their convex hull can only have triangles as its faces. This implies that the faces of the SCHull graph are all triangular, and triangles are inherently convex.

## G ALGORITHMS AND ARCHITECTURE DETAILS

### G.1 GRAPH CONSTRUCTION ALGORITHMS

**Radial cutoff.** The Radial cutoff graph construction is implemented using the PyTorchGeometric (Fey & Lenssen, 2019) data transform `RadiusGraph`. This constructs the set of edges  $\{e_{ij} \mid \|x_i - x_j\| < r\}$  for a fixed radius  $r$ . In the NestedSquares dataset  $r = 4$ , this is the side length of the outer square. In all other tasks, where the baseline models use `RadiusGraph` to construct the graph, we use the default radius  $r$ .

**$k$ NN.** The  $k$ NN graph construction is implemented using the PyTorchGeometric (Fey & Lenssen, 2019) data transform `KNNGraph`. This constructs a directed set of edges such that each node has exactly  $k$  neighbors. The graph is then made undirected. In all tasks  $k = 3$ .

**Voronoi.** The Voronoi graph construction is implemented using the SciPy (Virtanen et al., 2020) spatial transform `Voronoi`. This constructs an undirected graph from the ridges of the Voronoi diagram.

## 1242 G.2 MESSAGE PASSING NEURAL NETWORK

1243

1244 The following message passing neural network:

1245

$$1246 \mathbf{m}_{ij} = \phi_m(\mathbf{h}_i^l, \mathbf{h}_j^l, e_{ij})$$

1247

$$1248 \mathbf{m}_i = \sum_{j \in \mathcal{N}(i)} \mathbf{m}_{ij}$$

1249

$$1250 \mathbf{h}_i^{l+1} = \phi_h(\mathbf{h}_i^l, \mathbf{m}_i)$$

1251

1252 is used for the experiments in Section 3.3. In particular, for the architecture MPNN+SCHull, we  
 1253 utilize the attributed version of SCHull defined in equation (5). For the base MPNN architecture, the  
 1254 edge attributes are discarded, i.e.,  $\mathbf{m}_{ij} = \phi_m(\mathbf{h}_i^l, \mathbf{h}_j^l)$ .

1255

1256

## 1257 H BENCHMARK DETAILS

1258

1259

1260

1261

1262

1263

1264

1265

1266

1267

1268

1269

1270

1271

1272

1273

1274

1275

1276

1277

1278

1279

1280

1281

1282

1283

1284

1285

1286

1287

1288

1289

1290

1291

1292

1293

1294

1295

1296

1297

1298

1299

1300

1301

1302

1303

1304

1305

1306

1307

1308

1309

### 1256 H BENCHMARK DETAILS

#### 1258 H.1 NESTEDSQUARES

1260 The NestedSquares dataset is a graph property prediction task designed to test the expressivity of  
 1261 geometric GNNs. The training, validation, and test splits contain rotated graphs depicted in Fig. 4.  
 1262 There are 6 training graphs, 2 test graphs, and 2 validation graphs, and they contain randomly rotated  
 1263 graphs. The training procedure uses the Adam optimizer to minimize the mean squared error (MSE)  
 1264 loss between the model predictions and ground truth graph labels. The training uses the Adam  
 1265 optimizer with a learning rate of  $1e-4$  and a learning rate scheduler, which reduces by a factor of 0.9,  
 1266 has a patience of 25, and a minimum lr of  $1e-5$ . The model is trained for 100 epochs, with the test  
 1267 loss reported for the epoch with the best validation loss.

#### 1268 H.2 MD17

1270 The MD17 dataset is a node property prediction task, which contains a variety of molecular dynamics  
 1271 trajectories. Both the training and validation sets contain 1K samples, with the remaining data used for  
 1272 testing. The training procedure uses the Adam optimizer to minimize the L1 loss between the model  
 1273 predictions and ground truth molecular energy and forces. The training uses the Adam optimizer  
 1274 with a learning rate of  $5e-4$  and a learning rate scheduler which reduces by a factor of 0.5 and has a  
 1275 patience of 50. The model is trained for 1100 epochs, with the test loss reported for the final epoch.

#### 1277 H.3 PROTEIN DATASET

1279 **Fold dataset.** We utilize the same dataset as that used by Hou et al. (2018); Wang et al. (2022a).  
 1280 The dataset includes 16,292 proteins across 1,195 folds. To assess generalization performance, three  
 1281 test sets are employed: Fold, where proteins from the same superfamily are excluded from training;  
 1282 Superfamily, where proteins from the same family are not included in training; and Family, where  
 1283 proteins from the same family are part of the training data. Among these, Fold poses the greatest  
 1284 challenge, as its proteins differ the most from those in the training set. For this task, 12,312 proteins  
 1285 are used for training, 736 for validation, 718 for Fold, 1,254 for Superfamily, and 1,272 for Family.

1286 **Reaction dataset.** For the reaction classification task, 3D structures of 37,428 proteins corresponding  
 1287 to 384 EC numbers are obtained from PDB (Berman et al., 2000), with EC annotations for each  
 1288 protein retrieved from the SIFTS database (Dana et al., 2019). The dataset is divided into 29,215  
 1289 proteins for training, 2,562 for validation, and 5,651 for testing. Each EC number is represented  
 1290 across all three splits, and protein chains sharing more than 50% sequence similarity are grouped  
 1291 together.

1292 **LBA dataset.** Following (Jing et al., 2020), we perform ligand binding affinity predictions on a subset  
 1293 of the commonly-used PDBbind refined set (Wang et al., 2004; Liu et al., 2015). The curated dataset  
 1294 of 3,507 complexes is split into train/val/test splits based on a 30% sequence identity threshold to  
 1295 verify the model generalization ability for unseen proteins. For a protein-ligand complex, we predict  
 the negative log-transformed binding affinity  $pK = -\log_{10}(K)$  in Molar units.

## I HYPERPARAMETER DETAILS

### I.1 NESTEDSQUARES

Table 9 reports the hyperparameters for each invariant GNN which are adjusted from the baseline models. Additionally, we find that models are particularly sensitive to the cutoff which serves as a soft threshold parameter in each of the models. We report the results from the best cutoff using a grid search from 1 to 10. The chosen cutoff parameter is reported in Table 10.

	hidden_features	num_radial	num_spherical
DimeNet++	128	6	7
SphereNet	256	6	7
ComENet	128	8	8
MPNN+SCHull	256	32	3

Table 9: Hyperparameter selection for the NestedSquares dataset.

	Radial cutoff	$k$ NN ( $k = 3$ )	Voronoi	SCHull (ours)
MPNN	8	6	7	8
DimeNet++	3	3	3	—
SphereNet	9	9	9	—
ComENet	8	8	7	—

Table 10: Cutoff hyperparameter in the NestedSquares task for each model and graph connectivity.

### I.2 MD17

Model and training hyperparameters for the MD17 task are listed in Table 11.

Hyperparameter	Values/Search Space
Number of layers	4, 6
Hidden channels	256
Number of radial basis	32, 64
Cutoff	6, 8, 10
Epochs	1200
Batch size	64
Learning rate	5e-4
Learning rate scheduler	steplr
Learning rate decay factor	0.5
Learning rate decay epochs	180
Weight decay rate	1e-12

Table 11: Model and training hyperparameters search space for MD17 tasks.

### I.3 PROTEIN DATASET

Model and training hyperparameters search space for the protein tasks are listed in Table 12

Hyperparameter	Values/Search Space		
	React	Fold	LBA
Number of layers	3, 4, 5	3, 4, 5	3, 4, 5
Hidden channels	64, 128, 256	64, 128, 256	128, 192, 256
Cutoff	6, 8, 10	6, 8, 10	6, 8, 10
SCHull+Cutoff	6, 7, 8	6, 7, 8	6, 8
Dropout	0.2, 0.3, 0.5	0.2, 0.3, 0.5	0.2, 0.3
Epochs	500, 1000	500, 1000	300, 500
Batch size	16, 32	16, 32	8, 16, 32
Learning rate	1e-4, 5e-4	1e-4, 5e-4	5e-5, 1e-4, 2e-4
Learning rate scheduler	steplr	steplr	steplr
Learning rate decay factor	0.5	0.5	0.5
Learning rate decay epochs	50, 100	100, 200	50, 100

Table 12: Model and training hyperparameters for protein-related datasets.